Anomalous transport in U(1)-symmetric quantum circuits

Alessandro Summer,[1, 2, *] Alexander Nico-Katz,[1, 2, †] Shane Dooley,[3, ‡] and John Goold[1, 2, 4, §]

[1]*School of Physics, Trinity College Dublin, Dublin 2, Ireland*
[2]*Trinity Quantum Alliance, Unit 16, Trinity Technology and Enterprise Centre, Pearse Street, D02 YN67, Dublin 2, Ireland*
[3]*Dublin Institute for Advanced Studies, School of Theoretical Physics, 10 Burlington road, Dublin, D04 C932, Ireland*
[4]*Algorithmiq Ltd, Kanavakatu 3C 00160, Helsinki, Finland*
(Dated: November 22, 2024)

In this work we investigate discrete-time transport in a generic $U(1)$-symmetric disordered model tuned across an array of different dynamical regimes. We develop an aggregate quantity, a circular statistical moment, which is a simple function of the magnetization profile and which elegantly captures transport properties of the system. From this quantity we extract transport exponents, revealing behaviors across the phase diagram consistent with localized, diffusive, and - most interestingly for a disordered system - superdiffusive regimes. Investigation of this superdiffusive regime reveals the existence of a prethermal "swappy" regime unique to discrete-time systems in which excitations propagate coherently; even in the presence of strong disorder.

I. INTRODUCTION

The advent of large-scale, high-fidelity, tunable, and accessible digital quantum devices is revolutionizing modern quantum physics. Notable advances include the implementation of large-scale quantum algorithms, the simulation (via e.g. the Suzuki-Trotter expansion [1, 2]) of continuous-time models on actual hardware [3–8], diagonalization algorithms [9, 10], and the analysis of transport properties [11–14].

However, these advances have also resulted in an emerging reconceptualization of large circuits as realizing digital phases of matter *in their own right*. Notable examples include: discrete time crystals [15, 16], measurement induced phase transitions [17–19], many body scars [20, 21], Hilbert space fragmentation [22–24], and cellular automata [25]. Essentially, despite their fundamental differences, a sufficiently large discrete system exhibits emergent phenomena in a manner consistent with continuous phases of matter. This deterritorialization of phase, now encompassing digital systems, yields questions of immediate interest and relevance: how can one probe phase transitions and information-spreading in digital matter? As digital systems do not conserve energy, but can sustain other conserved quantities, what are the transport features of such systems? Are there additional regimes and features unique to digital phases of matter, absent in their continuous-time counterparts?

In this work, we seek to address some of these questions by constructing a generic gate-based, disordered, $U(1)$-symmetric model; inspired by the more recent development of a discrete-time version of the XXZ spin chain [26–28]. The continuous-time XXZ model, and its isotropic counterpart the Heisenberg model, were
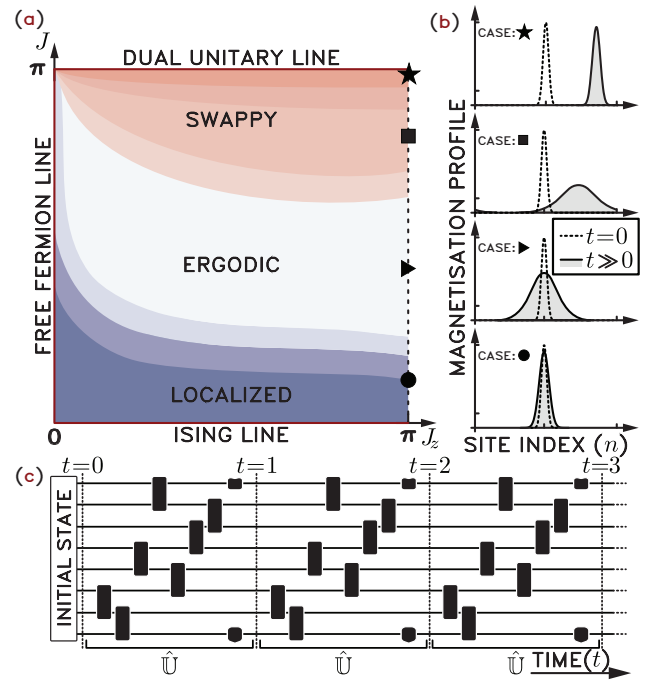

FIG. 1. Schematics showing (a) different regimes of our generic $U(1)$-symmetric model. Along the three solid borders the model is integrable; whilst the dashed border at $J_z = \pi$ spans four distinct regimes, and is the region we predominantly address in this article. (b) shows the initial (dotted) and late-time (solid) spin magnetization profiles for different phases along the $J_z = \pi$ line. (c) shows discrete time evolution as determined by a (periodic) $U(1)$-symmetric Floquet unitary $\hat{\mathbb{U}}$ comprised of nearest-neighbour gates.

conceived as purely theoretical constructs [29], but have become standard tools for investigating transport properties [30–32] and many-body localization (MBL) [33–43]. Meanwhile, the transport properties of its discrete-time counterpart remain only partially mapped out. Our model can be tuned across a two-dimensional phase space to exhibit a both integrable and non-

integrable regimes, and a range of emergent phenomena. This includes a crossover between ergodic and localized regimes [44], and a line along which all gates in our model are dual-unitary (DU) [45, 46]. These DU gates are endowed with an additional $U(1)$ symmetry, and thus become generalized SWAP gates (see Sec. III). We leverage our model into an investigation of the static properties of our model, revealing no unexpected behavior. However, we subsequently interrogate transport in our model and identify a prethermal regime which is *a priori* unique to discrete systems, in the vicinity of the DU line. In this regime, which we call the "swappy" regime due to its vicinity to the generalized SWAPs on the DU line, excitations propagate faster than in the ergodic phase, resulting in rapid coherent information transport over short timescales. Finally, by deploying circular moments related to wrapped probability distributions, we develop an aggregate quantity, R, which captures the features of many-body transport in a concise way. As this quantity is singularly composed of local Z-basis expectation values, it is highly amenable to experimental implementation; paving the way for the near-future experimental analysis of transport in digital matter.

In Sec. II, we present our model and compare it with similar ones. Sec. III outlines the primary features anticipated to appear in our phase diagram, as suggested by the existing literature. Sec. IV reports the results: Sec. IV A for static properties obtained via exact diagonalization and Sec. IV B for dynamical properties that define the finite time and size transport analysis of our model.

II. MODEL

We consider a system of N qubits undergoing discrete-time evolution under the repeated application of a Floquet unitary $\hat{\mathbb{U}}$. The Floquet unitary is decomposed as product of N nearest-neighbour gates $\hat{\mathbb{U}} = \prod_{\{P(n)\}} \hat{U}_{n,n+1}$, ordered according to a random permutation P of the set of all site indices n (illustrated in Fig. 1(c)). We assume periodic boundary conditions. The two-qubit gates have the form:

$$\hat{U}_{n,n+1} = e^{-i\hat{H}_{n,n+1}} e^{-ih_n \hat{S}_n^z} e^{-ih'_n \hat{S}_{n+1}^z}, \qquad (1)$$

which is composed of the single-qubit rotations $e^{-ih_n \hat{S}_n^z} e^{-ih'_n \hat{S}_{n+1}^z}$ and a nearest-neighbour XXZ-like interaction generated by the Hamiltonian:

$$\hat{H}_{n,n+1} = \frac{J}{2} \left(\hat{S}_n^+ \hat{S}_{n+1}^- e^{i\phi_n} + \hat{S}_n^- \hat{S}_{n+1}^+ e^{-i\phi_n} \right) + J_z \hat{S}_n^z \hat{S}_{n+1}^z, \qquad (2)$$

with the Peierls phase ϕ_n [47]. Here, the operators $\hat{S}_n^\alpha$ for $\alpha \in \{x, y, z\}$ are the standard spin-1/2 operators acting locally on the n'th site, and the raising and lowering operators are defined as $\hat{S}_n^\pm = \hat{S}_n^x \pm i\hat{S}_n^y$ respectively. The two-qubit gate in Eq. (1), with five parameters $\{h_n, h'_n, \phi_n, J, J_z\}$, can, in fact, describe any two-qubit gate that conserves the total magnetization $\hat{M} = \sum_n \hat{S}_n^z$ in the z-direction . Since each individual gate conserves the magnetization, the global Floquet unitary also conserves the total magnetization $[\hat{\mathbb{U}}, \hat{M}] = 0$, which is an essential prerequisite to define the transport of spin excitations.

For each two-qubit gate $\hat{U}_{n,n+1}$ we sample the three phase parameters $\{h_n, h'_n, \phi_n\}$ randomly from the uniform distribution on the interval $[-\pi, \pi]$. This introduces disorder to our circuit model. The two remaining parameters J and J_z, however, are fixed across all gates in a given Floquet unitary. Tuning J and J_z allows us to explore various regimes of transport in our model. Observing that the two-qubit gate $\hat{U}_{n,n+1}$ is 2π-periodic in both J and J_z we can restrict our parameter space through patterning (reflection and tessellation) to the region $J, J_z \in [0, \pi]$, shown in Fig. 1(a).

Similar discrete-time models have appeared in recent literature [44, 48–56]. Notably, Refs. [44, 54–56] use $U(1)$ symmetric models but with a brickwork geometry. Our random gate ordering is more similar to the approach in Ref. [50]. This approach also allows systems with odd and even site numbers, N, to be treated equivalently and avoids issues related to the slower thermalization of brickwork circuits, as discussed in Ref. [56]. A more in-depth analysis of gate permutations is presented in App. A. Finally, we note that our model is well-suited to for realization on currently available quantum hardware. A different gate decomposition of $\hat{U}_{n,n+1}$ which may be more suitable for implementation on quantum simulators is discussed in App. C.

III. OVERVIEW OF REGIMES OF TRANSPORT DYNAMICS

Before presenting our numerical results, in this section we give an overview of the expected different regimes of dynamics in our model. First, we identify three solvable regimes of our model, corresponding to three solid borders of the $J, J_z \in [0, \pi]$ square in Fig. 1(a):

1. If $J_z = 0$ the Floquet unitary is integrable, since it can be mapped to a quadratic fermion model by a Jordan-Wigner transformation.

2. If $J = 0$ the Floquet unitary reduces to an Ising model in a disordered longitudinal magnetic field, since it is completely diagonal in the $\hat{S}_n^z$ basis of each spin.

3. If $J = \pi$ each gate of our model is DU. In what follows we show that imposing $U(1)$ symmetry to DU gates leads to generalized SWAP gates making the system effectively non-interacting and therefore integrable.

In the first of these regimes, along the free-fermion line $J_z = 0$, we expect transport to by suppressed by Anderson localization, as a result of the disorder fields $\{h_n, h'_n, \phi_n\}$. Similarly, in the second of the exactly solvable regimes, along the Ising line, there is no transport of spin-z excitations since, at $J = 0$, not only is the total magnetization $\hat{M}$ conserved, but also the local magnetization $\hat{S}^z_n$ for every spin n is conserved.

We now turn our attention to the third of our exactly solvable regimes, at $J = \pi$, where the two-qubit gate can be decomposed as:

$$
\begin{aligned}
\hat{U}_{n,n+1} =& e^{-i\kappa_+}|\uparrow\uparrow\rangle\langle\uparrow\uparrow| + e^{-i\xi_+}|\downarrow\uparrow\rangle\langle\uparrow\downarrow| \\
& + e^{-i\xi_-}|\uparrow\downarrow\rangle\langle\downarrow\uparrow| + e^{-i\kappa_-}|\downarrow\downarrow\rangle\langle\downarrow\downarrow|,
\end{aligned}
\tag{3}
$$

for $\kappa_\pm = \mp(h + h')/2 + J_z/4$ and $\xi_\pm = \pi \pm (h - h')/2 - J_z/4 \mp \phi$. We see that, along this line in parameter space, our two-qubit gate becomes a SWAP gate that also imprints a phase on the swapped particles. We will refer to this gate as a generalized SWAP and to the $J = J = \pi$ point as the "SWAP point". This use of the term is justified within the context of the Weyl chamber, where gates connected by local rotations are defined as equivalent [51, 57]. Hence, we do not expect the system to thermalize along the DU line, as any spin excitation propagates through the circuit unimpeded via a series of these generalized SWAP gates. The intrinsic behavior of this type of gate ensures that any DU circuit preserving $U(1)$ symmetry is integrable, regardless of connectivity.

The non-thermalizing behavior along these three borders raises several interesting questions about the dynamics if we vary slightly away from them. Traditionally this has been studied in the proximity of the Ising line. Even if we perturb away from it, by increasing J to small but non-zero values, spin transport is still suppressed, since the kinetic energy J-term in Eq. (2) is dominated by the disorder fields $\{h_n, h'_n, \phi_n\}$. This is roughly analogous to MBL in continuous-time models [35, 58] but, as MBL is not the main focus of this article, we do not interrogate the stability of this regime in the thermodynamic limit. However one can wonder if something similar can arise around the DU line. Will the system thermalize near it? Is there an extended regime of anomalous transport dynamics near the DU line? These are some of the key motivating questions of our work. We will show below that indeed there is a distinctive regime of anomalous transport proximate to the DU line, which we will call the "swappy" regime. Moving further away from the three solvable sides of our $J, J_z \in [0, \pi]$ square, we enter the ergodic regime. Here, we expect transport of spin excitations to lead to rapid thermalization of the system.

To explore the behavior of our model between the Ising and the DU line, we focus on the $J_z = \pi$ line, since it is maximally distant (in (J, J_z) parameter space) from the integrable free-fermion line, and exhibits a wide array of interesting behaviors as a function of the single parameter J. In particular, throughout this work we focus on four points representative of the different regimes along this line: localized at $J = 0.395$ (represented by the symbol ●), ergodic at $J = 1.374$ (represented by ▶), swappy at $J = 2.551$ (represented by ■), and near-SWAP at $J = 3.138$ (represented by ★). These regimes are shown schematically in Fig. 1(b). These regimes exhibit different kinds of emergent transport and, as we flexibly refer to regimes and types of transport throughout this work, it is instructive to preemptively summarize our findings here. We find either complete localization or sub-diffusive behavior in the localized regime, diffusive behavior in the ergodic regime, and super-diffusive behavior in the swappy and near-SWAP regime. This super-diffusive behavior is augmented by ballistic propagation of individual excitations in the swappy and near-SWAP regimes. These results are shown in Fig. 5 and Fig. 6, and discussed in Sec. IV B 3 and Sec. IV B 4 respectively.

We emphasize that a full scaling analysis of the localized regime falls outside the scope of this work, and due to analogous literature surrounding the stability of continuous-time MBL, we expect this question to be intractable given current numerical and experimental capabilities [58, 59]. We can thus only claim to find phenomenological signatures of localization in this work: i.e. a total breakdown of transport, or the sub-diffusive (and/or logarithmic) spreading of information. These phenomenological signatures may be prethermal effects, or finite-size size effects, or both; we defer a more detailed investigation of the stability of localization in discrete-time systems to future study. In this work we focus on phenomenological signatures of transport throughout the phase diagram, at intermediate system sizes $N \leq 22$, and exponential timescales; with an additional focus on interrogating the nature and stability of the swappy regime.

IV. RESULTS AND ANALYSIS

Our goal in this paper is to understand the various equilibrium and dynamical regimes in our $U(1)$-symmetric circuit model, outlined in the previous section. To characterize our model, we take two complementary approaches: we compute (Sec. IV A) static spectral properties and (Sec. IV B) dynamical properties. These two approaches are complementary, since they reveal different aspects of the model, as described below.

A. Spectral properties

One way to characterize our model is by means of its spectral properties, i.e, properties relating to the eigenphases and eigenvectors of the Floquet unitary, $\hat{\mathbb{U}}|\varphi_i\rangle = e^{-i\varphi_i}|\varphi_i\rangle$. Specifically, we study the mean eigenstate entanglement entropy and the mean eigenvalue gap ratio—both indicators of quantum chaos [58].
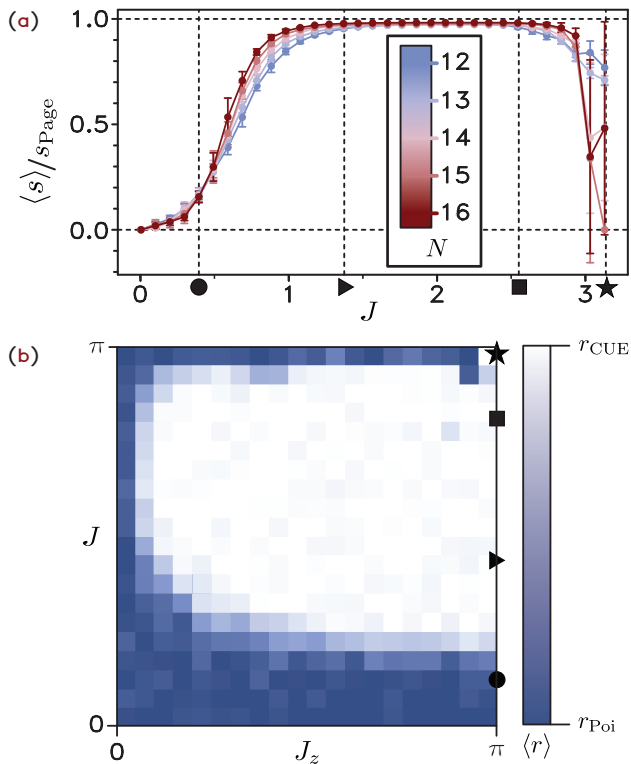
FIG. 2. Static properties of the model are shown. In (a) (top) shows results for the averaged von Neumann entanglement entropy normalized by the Page value, along the $J_z = \pi$ line and for various system sizes. Values were averaged over $20 - 35$ trajectories. (b) (bottom) displays the phase diagram for the gap ratio obtained for $N = 15$ with values averaged over $10 - 20$ trajectories.

First, consider a bipartition of the system into subsystems A and B. The entanglement entropy of a Floquet eigenstate $|\varphi_i\rangle$ is given by:

$$s_i = -\text{Tr}[\hat{\rho}_i^A \ln(\hat{\rho}_i^A)], \tag{4}$$

where $\hat{\rho}_i^A = \text{Tr}_B[|\varphi_i\rangle\langle\varphi_i|]$ is the reduced density matrix for subsystem A. Averaging s_i over eigenstates in a fixed magnetization sector M (see App. B) and across different Floquet unitaries yields the mean entanglement entropy $\langle s \rangle$. For an ergodic system we expect the eigenstates to have an average entanglement entropy similar to a typical random state in the magnetization sector, i.e., close to the Page entropy $s_{\text{Page}} = \ln d_A - d_A^2/2d$, where d is the total Hilbert space dimension and d_A is the dimension of subsystem A [60], as discussed in App. B. For this reason, it is sometimes convenient to normalize the average entropy by the Page entropy, $\langle s \rangle / s_{\text{Page}}$. In Fig. 2(a) we see that, for our model, the mean entanglement entropy varies from a small value in the localized regime ($J \ll \pi$) to the Page entropy in the ergodic regime. This is consistent with the conclusion that – at least for our finite-N – the system fails to thermalize in the long-time limit in the localized regime, but thermalizes in the ergodic regime. Fig. 2(a) also appears to show deviations

from the Page entropy as we approach the SWAP point $J \to \pi$. However, we observe that as the system size N increases, the range of J values around π associated with lower entanglement entropy contracts.

Our next quantifier is the mean gap ratio. For each Floquet eigenphase φ_i, the ratio of consecutive gaps is defined as:

$$r_i = \frac{\min\{\delta\varphi_{i-1}, \delta\varphi_i\}}{\max\{\delta\varphi_{i-1}, \delta\varphi_i\}}, \tag{5}$$

where $\delta\varphi_i = \varphi_{i+1} - \varphi_i$ is the gap between consecutive eigenphases within the same magnetization sector [61]. We compute the mean gap ratio $\langle r \rangle$ by averaging r_i over all eigenphases in a sector and over many Floquet unitaries. In the absence of time-reversal symmetry, the model is expected to yield $\langle r \rangle \approx r_{\text{CUE}} = 0.6027$ if the system is ergodic, or $\langle r \rangle \approx r_{\text{Poi}} = 0.3863$ if the system is integrable [62]. Fig. 2(b) shows the transition between the localized regime for small J and the ergodic regime for sufficiently large J. It also shows a deviation from the ergodic value when $J_z = 0$, corresponding to our model being integrable (mappable to free fermions), as well as on the dual-unitary line $J = \pi$.

Both the mean entanglement entropy and the mean gap ratio probe equilibrium properties of the model in the infinite time limit. So, even if the system ultimately thermalizes, interesting intermediate-time behaviors may arise which will not be detected by these spectral quantities. Next we turn to quantification of the transport properties of the model, which can reveal distinct dynamical regimes at intermediate times.

B. Transport properties

In Sec. IV B 1 we first present the raw numerical data for the evolution of the local magnetization profile, starting from a non-equilibrium initial state consisting of a localized spin excitation in a homogeneous spin background. Suitably quantifying the spread of the the initially localized excitation should encapsulate the transport properties of the system. However, we find that the local magnetization profile is inconvenient for extracting transport coefficients. In section Sec. IV B 2 we map the local local magnetization profile to a quasi-probability distribution. Using the wrapped normal distribution as a helpful reference model, we use the quasi-probability distribution to extract transport coefficients. These transport coefficients are discussed in section Sec. IV B 3. Finally, in Sec. IV B 4, we conduct a scaling analysis of the transport properties. This study reveals an intermediate-time prethermal "swappy" regime, unique to digital systems, where information propagates coherently and ballistically, even in a strongly disordered setting. We discuss heuristic mechanisms underlying this regime, and its stability, in Sec. IV B 5.

1. Local magnetization profile

The central object used to explore dynamics in our model is the local spin magnetization profile

$$M_n(t) = \text{Tr}[\hat{\mathbb{U}}^t \hat{\rho}(0)(\hat{\mathbb{U}}^\dagger)^t \hat{S}_n^z]. \qquad (6)$$

We exploit initial states of the form

$$\hat{\rho}(0) = \hat{P}_M \left[|\uparrow\rangle\langle\uparrow|_{N/2} \otimes \left(\frac{\hat{\mathbb{1}}_2}{2} \right)^{\otimes(N-1)} \right] \hat{P}_M, \qquad (7)$$

where $\hat{P}_M$ is a projector onto the subspace of total magnetization $M = \sum_n M_n$. In numerical practice, to avoid working with the density matrix $\hat{\rho}(0)$ in Eq. (6), we choose the initial pure state $\hat{\rho}(0) \sim \hat{P}_{N/2}^\uparrow |\psi_{\text{rand}}\rangle\langle\psi_{\text{rand}}|\hat{P}_{N/2}^\uparrow$ where $|\psi_{\text{rand}}\rangle$ is a random state in the subspace of fixed total magnetization M, and $\hat{P}_{N/2}^\uparrow$ is the projector onto the excited state of the middle spin. This is numerically more efficient, since we only need to operate on the pure state instead of on the density matrix. In App. F 1 we show in detail that this is equivalent to choosing an initial maximally-mixed state in Eq. (6), up to some negligible random fluctuations. Notably, one can directly connect the quantity of eq. (6) computed in a given magnetization subsector with high-temperature correlation functions, as is shown in detail in app. F.

For this choice of initial state, the central spin is fully polarized such that $M_{N/2}(0) = 1/2$. The excess magnetization $M - 1/2$, where $M = \sum_n M_n(t)$, is distributed evenly over all other spins $M_{n \neq N/2}(0) \approx M_{\text{B}} = (M - 1/2)/(N - 1)$. In other words, the initial local magnetization is in the non-equilibrium configuration:

$$M_n(0) = \frac{1}{2}\delta_{n,N/2} + (1 - \delta_{n,N/2})M_{\text{B}}. \qquad (8)$$

As total magnetization M is conserved in our model, and as thermalization would result in the initially localized spin excitation spreading through the system, full thermalization corresponds to the total magnetization M being uniformly distributed across all spins $M_n(t \to \infty) \approx M/N$. As is standard, we focus on the largest subsector: taking $M = 0$ from this point onward.

We present our numerical results for the magnetization profile $M_n(t)$ for a system of $N = 20$ particles in Fig. 3 at the four key points along the $J_z = \pi$ line (as shown in Fig. 1(a)). The top panels (a-d) illustrate the dynamics for a typical individual realization of $\hat{\mathbb{U}}$, while the bottom panels (e-h) show the dynamics of the local magnetization averaged over many different realizations of the Floquet unitary.

As outlined in Sec. II, and depicted in Fig. 1(c), time evolution is carried out by repeated application of the Floquet unitary $\hat{\mathbb{U}}$. We evaluate each of the first $t = 100$ time steps, but to reach later times we apply clusters of Floquet unitaries together $\hat{\mathbb{U}}^k$, which effectively realizes a stroboscopic dynamics with a longer period after

$t > 100$. This stroboscopic approach leads to an apparent preservation of excitation on some particular sites, however even at this later times we expect the excitation to move continuously along the chain. Throughout Fig. 3, horizontal lines mark (solid) $t = 1$, the application of the first whole $\hat{\mathbb{U}}$, (dashed) $t = N/2 = 10$, the time for ballistic excitations to reach the system boundary, and (dotted) $t = (N/2)^2 = 100$, the time taken for a particle on site $N/2$ to diffuse to the boundary of the system. These three benchmarks help compare different types of transport, where the $t = 100$ line serves as a reference for identifying diffusive or anomalous behavior. White regions denote homogenized $M_n(t) = 0$, indicating regions in which the state realizes a local identity and has self-thermalized.

In the localized regime (●), shown in (a) and (e), the initial spin excitation remains localized for a long-term, preserving its general shape and position in the spin chain. The system exhibits self-averaging at late times (i.e., after the early-time relaxation dynamics), consistent with many-body localization studies [35, 63–65]. Self-averaging means a system's properties become stable and predictable in large samples without many different realizations. This feature breaks down in phase transitions where disorder causes persistent fluctuations across regions, preventing uniform behavior. The initial excitation spread slowly, likely logarithmically, in line with what usually marked as localized behavior [58, 59, 64, 66].

In the ergodic regime (▶), shown in (b) and (f), diffusive transport is qualitatively evidenced by the excitation reaching the boundary, and the subsequent onset of thermalization, at time $t = 100$ (the dotted black line). Also at this point self-averaging occurs, with individual realizations (b) resembling the averaged behavior (f).

The swappy regime (■) is displayed in panels (c) and (g). The individual realization in panel (c) demonstrates a clear leftward propagation of the initial excitation, with the direction determined randomly by the permutation P of the local gates making up the Floquet unitary. Initially, before the small deviations from the SWAP gate become evident, the excitation propagates coherently and ballistically through the system, moving a fixed number of sites per Floquet cycle. We will later quantify this behavior using the instantaneous speed parameter $\langle\nu\rangle$ in Sec. IV B 4. These ballistic excitations eventually decohere, leading to thermalization after roughly 10 Floquet applications. This fast thermalization is more apparent in the averaged dynamics of panel (g), where excitations propagate in both directions, splitting into "twin peaks." These excitations self-interact and thermalize rapidly after $t \sim 10$. This finding is significant: thermalization occurs on a timescale consistent with *ballistic* transport in a disordered quantum system. Such anomalous transport has been observed in disorder-less models (see Refs. [26–28]), but here we find counter-intuitive evidence of such behavior in strongly disordered systems.

Near the SWAP point (★), panel (d) clearly shows the leftward propagation of the initial excitation. However in
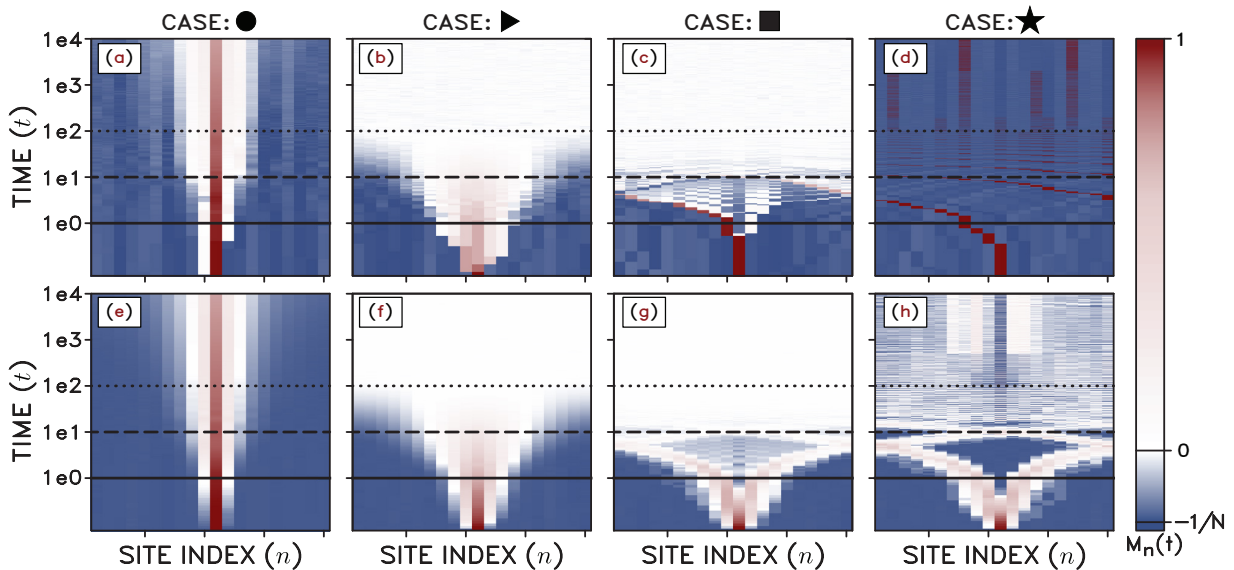
FIG. 3. Results of numerical propagation of the initial spin inhomogeneity in the $M = 0$ sector under $U(1)$-symmetric Floquet dynamics at $N = 20$. Panels (a)-(d) show typical results for single realizations of the initial state and Floquet unitary within the localized regime, ergodic regime, and two points in the swappy regime respectively. Panels (e)-(h) show results in the respective regimes after averaging over 100 realizations. Horizontal lines indicate the time taken to complete a single Floquet cycle (solid), $N/2$ (dashed), and the time after which we calculate results stroboscopically (dotted).

this case the system continues to exhibit a near-perfect exchange of spin excitations with neighboring sites, even at late times. Panel (h) appears to show thermalization at late times. However, this is actually the result of averaging out the peak, caused by small variations in the underlying propagation speeds. Essentially, while the center of $M_n(t)$ shifts, its initial delta-peaked functional form remains unchanged. Averaging many such randomly centered delta-peaked distributions creates the appearance of thermalization at late times. Once again, we observe an early-time "twin peaks" structure, where the excitation propagates coherently and ballistically in both directions. Unlike in most of the swappy regime, the twin peaks here are well-resolved. The absence of full thermalization at the near-SWAP point is likely due to the timescales accessed; with a complete failure to thermalize at all times associated only with the SWAP point $J = \pi$.

2. Mapping local magnetization to a quasi-probability

To gain a deeper understanding of the transport dynamics of the initially localized excitation: we first construct a statistical moment derived from the magnetization profile. From this moment we can extract transport properties (namely transport exponents and drift) which can in turn be related (via an appropriate choice of initial state) to high-temperature correlation functions (see App. F).

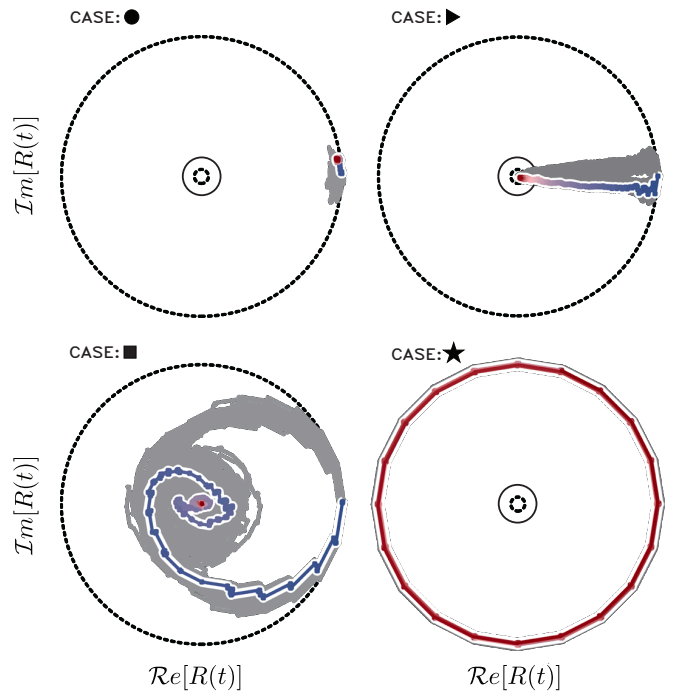To this end, we first construct a quasi-probability distribution $p_n(t)$ by transforming the magnetization profile

FIG. 4. Representations of $R(t)$ on the complex plane, within the unitary circle, are shown for the following values of J: (●) $J = 0.395$ (localized), (▶) $J = 1.374$ (ergodic), (■) $J = 2.551$ (swappy), and (★) $J = 3.138$ (near-SWAP regime). A typical trajectory from the total $\Omega = 100$ trajectories is highlighted with a gradient from blue to red, corresponding to t from 0 to 100, and $N = 20$. The remaining trajectories are displayed in grey.

$M_n(t)$ as follows:

$$p_n(t) = 2\frac{M_n(t) - M_{\mathrm{B}}}{1 - 2M_{\mathrm{B}}}. \tag{9}$$

This transformation approximately maps the initial background magnetization values to zero, $p_{n \neq N/2}(0) \approx 0$, with the excitation at $p_{N/2}(t) = 1$, and satisfies Kolmogorov's second probability axiom, $\sum_n p_n(t) = 1$, due to the $U(1)$ symmetry (i.e., conservation of M). Small fluctuations during the random initial state preparation may cause $M_n(t) < M_{\mathrm{B}}$, leading $p_{n \neq N/2}(0)$ to dip below zero. As a result, $p_n(t)$ technically becomes a quasi-probability distribution, violating Kolmogorov's first axiom. However, this effect is minimal and vanishes as $N \to \infty$. We observe no pathological behavior due to these small negative values, so we treat $p_n(t)$ as a valid probability distribution. Full thermalization, $M_n(t \to \infty) = M/N$, results in a uniform distribution, $p_n(t \to \infty) \approx 1/N$.

Since we assume periodic boundary conditions for our model, it is also convenient to introduce the circular mean; defined by the complex number:

$$R(t) = \sum_n p_n(t)e^{i\theta_n} = e^{i\mu(t) - \sigma(t)^2/2}, \tag{10}$$

where $\theta_n = \pi(n - N/2)/N \in [-\pi, \pi]$ maps the magnetization profile, via the quasi-probability distribution $p_n(t)$, of N spins to a single complex value within the unit circle $|R(t)| \leq 1$. Here, the parameters:

$$\mu(t) = \mathrm{Arg}[R(t)], \qquad \sigma(t) = \sqrt{-2\log[|R(t)|]} \geq 1, \tag{11}$$

quantify the position and the spread of the spin excitation, respectively. To see this intuitively, consider the example of a quasi-probability profile $p_n = \delta_{n,m}$ for a spin excitation localized at site $n = m$. It corresponds to the point $R = e^{i\theta_m}$ on the unit circle, with the argument $\mu = \theta_m$ reflecting the position m of the excitation and spread parameter $\sigma = 0$ indicating that the excitation is perfectly localized. At the opposite extreme, for the example of a completely delocalized spin excitation we have the quasi-probability profile $p_n = 1/N$. It corresponds to the point $R = 0$ at the origin of the unit circle, with the spread parameter $\sigma = \infty$ indicating that the excitation is completely delocalized (the argument μ is undefined in this case, since the excitation spread uniformly across the chain has no well-defined position). We can thus interpret $R(t)$ as a vector on the complex plane, where drift of the localized excitation corresponds to rotation of $R(t)$ about the origin, and delocalization corresponds to a shrinking of the magnitude of $R(t)$. Taken together, these allow us to conveniently visualize different kinds of transport dynamics on the unit circle: diffusion and thermalization cause $R(t)$ to move towards the origin, and coherent transport of an excitation through the system is realized as rapid rotation of $R(t)$ around the origin.

Our decision to characterize transport via the circular mean $R(t)$, and via $\mu(t)$ and $\sigma(t)$ as defined in Eq. (11) (rather than linear first and second moments of p_n [48, 67, 68]) is based on exploiting wrapped normal distributions as possible descriptions of systems with periodic boundary conditions. Our reasoning is as follows: the spreading of excitations in many-body systems is commonly modeled by a Gaussian distribution [69, 70]. This finds good correspondence with the classical diffusion equation, which in the one dimensional system is

$$\frac{\partial f}{\partial t} = D\frac{\partial^2 f}{\partial x^2}. \tag{12}$$

Here, an initial delta-function $f = \delta(x - x_0)$ (analogous to our initial state of Eq. (7)) experiences a decay of its peak $\sim t^{-1/2}$ and growth of the standard deviation as $\sim t^{1/2}$. Our model has periodic boundary conditions such that when the excitation, and thus the tails of the associated quasi-probability distribution, reach the boundary they 'wrap around' the edge and self-interact. The dynamics of the quasi-probability distribution can thus heuristically be captured by a wrapped normal distribution of the form:

$$\mathcal{N}_{\mathrm{W}}(n; \mu, \sigma) \propto \sum_{k=-\infty}^{\infty} \exp\left[\frac{-(\theta_n - \mu + 2\pi k)^2}{2\sigma^2}\right], \tag{13}$$

where the summation over k wraps the underlying normal distribution around the boundary, capturing the interactions of particles that diffuse across boundaries. For such a distribution, the bare parameters μ and σ in Eq. (13) are extracted precisely from the circular mean of Eq. (10) via Eq. (11). A potential limitation of this approach is that connection between $\sigma(t)$ and an underlying spread parameter of Eq. (13) only holds for systems which realize an approximately wrapped Gaussian form for their magnetization profiles. From Fig. 3 we see that this connection holds everywhere except in (c) and (g): the swappy regime, which exhibits the staggered patterning at early times which (see Sec. IV B 5). In this case, we instead exploit the mean position $\mu(t)$, from which we extract a drift speed in Sec. IV B 3, to characterize the swappy regime.

In Fig. 4 we show the dynamics of $R(t)$ for our the four regimes of our model for the first $t = 100$ time steps. We see that for the localized regime ($\bullet$), there is no transport of any kind, $R(t)$ remains close to its initial value for all times and trajectories. In the ergodic regime ($\blacktriangleright$), the trajectory exhibits rapid thermalization, $|R(t)| \to 0$, but no coherent information transport occurs. In the swappy regime ($\blacksquare$), coherent information transport is observed, as $\mathrm{Arg}[R(t)]$ varies at a relatively constant rate, in tandem with eventual thermalization, as $|R(t)| \to 0$. Finally, in the near-SWAP regime ($\star$), coherent information transport persists at a constant rate even at late times, with no noticeable equilibration, and $|R(t)|$ remains equal to 1 throughout.

3. Extracting transport properties

We are now prepared to quantitatively characterize the transport properties across our four distinct dynamical regimes. To assess the drift of the initial excitation, which is notably pronounced in the swappy and near-SWAP regimes, we define an instantaneous drift speed:

$$\nu(t) = \left| \frac{d\mu(t)}{dt} \right| \tag{14}$$

which, in practice, we modify slightly to account for discontinuities when excitations cross the boundary (see [71]). To further quantify the spread of the excitation, most prominently observed in the ergodic regime, we fit the parameter $\sigma(t)$ to the form:

$$\sigma(t) \sim t^{\alpha_\sigma}, \tag{15}$$

and determine the power-law exponent α_σ.

To quantify the decay of the initial excitation due to its spread through the system, we track the maximum value $p_{\max}(t) = \max_n p_n(t)$. This is fit to the form

$$p_{\max}(t) \sim t^{-\alpha_p}, \tag{16}$$

where α_p indicates the decay rate. As discussed in Sec. IV B 1, conventional diffusion corresponds to α_σ (or α_p) $= 1/2$, while ballistic transport aligns with α_σ (or α_p) $= 1$. Anomalous diffusion occurs with α_σ (or α_p) $< 1/2$ for subdiffusion and $> 1/2$ for superdiffusion.

From each trajectory $R(t)$, we derive the spread $\sigma(t)$ and drift speed $\nu(t)$ as per Eq. (11) and Eq. (14). Averaging over these realizations, denoted by $\langle A \rangle$, yields the sample-averaged spread $\langle \sigma(t) \rangle$ and speed $\langle \nu(t) \rangle$. Fig. 5 shows these averaged dynamics: (a) $\langle \sigma(t) \rangle$ and (b) $\langle \nu(t) \rangle$, for a range of values $J \in (0, \pi)$. The four points of interest are highlighted as bold black lines, labeled by their respective markers.

In Fig. 5(a), we compute the spread parameter $\langle \sigma(t) \rangle$ behavior. In the localized regime (●), information spreads slowly and logarithmically even at late times, analogously to MBL in continuous-time systems. In the ergodic regime (▶), $\langle \sigma(t) \rangle$ grows as $\sim t^{1/2}$, indicating diffusion until equilibration at $t \approx 10^2$, after which it saturates. The saturation of $\langle \sigma(t) \rangle$ to a constant contrasts with the expected divergence $\langle \sigma(t) \rangle \to \infty$ at equilibrium. However, App. E shows that this saturation is a finite-size effect vanishing as $N \to \infty$. The swappy regime (■) exhibits rapid thermalization: initially super-diffusive transport, $\langle \sigma(t) \rangle \sim t$, transitions to diffusion, $\langle \sigma(t) \rangle \sim t^{1/2}$, further explored in Fig. 5(c). In the near-SWAP regime (★), spread remains minimal, with only a slight late-time increase in $\langle \sigma(t) \rangle$.

In Fig. 5(b), the instantaneous transport speed $\langle \nu(t) \rangle$ highlights distinct behaviors across regimes. In the localized regime (●), no movement occurs, with $\langle \nu(t) \rangle \approx 0$ throughout. The ergodic regime (▶) shows non-zero speeds $\langle \nu(t) \rangle > 0$ at early times $t < 10$, but stabilizes

to $\langle \nu(t) \rangle \approx 0$ at later times. The swappy (■) and near-SWAP (★) regimes both display non-zero speeds for long times, with high values of $\langle \nu(t) \rangle$ persisting to extremely long times as $J \to \pi$ approaches the SWAP point. The peak of $\langle \nu(t) \rangle \approx 2$ aligns with the lightcone speed in brickwork circuits, reflecting the typicality of the permutation P and the Floquet unitary $\hat{U}$, as discussed in App. A. Calculations are limited to $t < 100$ to avoid unreliable speed estimates at stroboscopically sampled times.

In Fig. 5(c), we analyze the maximum value $\langle p_{\max}(t) \rangle$. Its behavior resembles that of $\langle \sigma(t) \rangle$ in Fig. 5(a) but inverted: high $\langle p_{\max}(t) \rangle$ values align with minimal spreading, while low values indicate a lack of spreading of the excitation. We see that, in the localized and near-SWAP regimes, $\langle p_{\max}(t) \rangle$ remains constant, or decays extremely slowly, since the spread of the excitation is suppressed. In the ergodic and swappy regimes, however, the decay of $\langle p_{\max}(t) \rangle$ is more rapid, consistent with the rapid spread of the excitation.

We note that, taken together, our three quantities $\langle \sigma(t) \rangle$, $\langle \nu(t) \rangle$ and $\langle p_{\max}(t) \rangle$ allow us to distinguish the dynamical behaviors in our various regimes. For instance, the spread $\langle \sigma(t) \rangle$ shows very similar behavior for both the swappy (■) and ergodic (▶) regimes, but these two regimes are clearly distinguished by the speed $\langle \nu(t) \rangle$. On the other hand, the speed $\langle \nu(t) \rangle$ does not easily distinguish the dynamical behaviors in the localised (●) and ergodic (▶) regimes, but these are easily distinguished with the quantity $\langle p_{\max}(t) \rangle$.

.

4. Extracting exponents

Here we process the realization-averaged spread, $\langle \sigma(t) \rangle$, the drift speed, $\langle \nu(t) \rangle$, and the peak decay, $\langle \sigma(t) \rangle$, to obtain quantities suitable for scaling analysis of transport properties across system sizes $N \in \{14, 16, 18, 20, 22\}$.

To determine the transport exponent α_σ from the transient behavior, $\langle \sigma(t) \rangle \sim t^{\alpha_\sigma}$, we focus on intermediate-time regions exhibiting stable log-log behavior (shaded in grey in Fig. 5(a)) [72].

The results of the exponent extraction process are displayed in Fig. 6(a). Two distinct flat regions emerge: one at $\alpha_\sigma = 0$ for very small J, and another at $\alpha_\sigma \approx 1/2$ as J increases through the ergodic regime. As discussed, the value $\alpha_\sigma = 1/2$ indicates diffusive transport, though from Fig. 6(a), it is unclear if α_σ stabilizes at this value as N grows. Larger systems sizes would also be required to determine if the smooth transitions between these flat regions sharpens with increasing system size N, which would indicate a clearly defined localized-ergodic crossover. However, our finite-N results are consistent with the static results in Fig. 2.

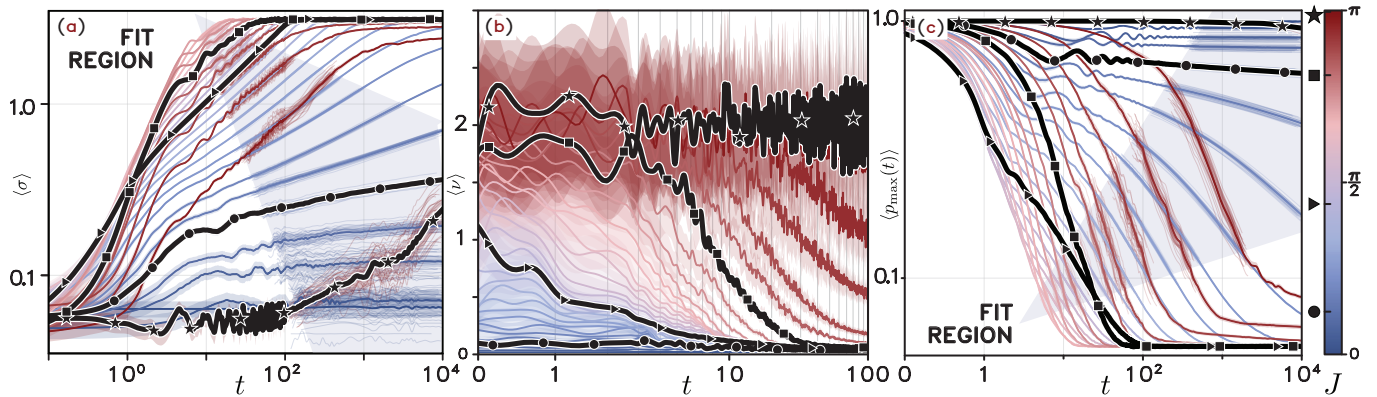In terms of transport properties, this behavior corre-

FIG. 5. The time evolution of the realization-averaged parameters for various values of $J \in (0, \pi)$, with $N = 20$ over 100 trajectories, is illustrated for: (a) the spread $\langle \sigma(t) \rangle$, (b) drift $\langle \nu(t) \rangle$, and (c) decay of $\langle p_{\max}(t) \rangle$. Four distinct regimes are marked with bold lines and symbols: (●) localized, (▶) ergodic, (■) swappy, and (★) near-SWAP. The grey-shaded areas in (a) and (c) highlight the time intervals used to fit the transport exponents α_σ and α_p, respectively. Due to stroboscopic sampling limitations, panel (b) is displayed only up to $t = 100$, effectively capturing all relevant behavior. Error bars are depicted as shaded semi-transparent regions where visible.
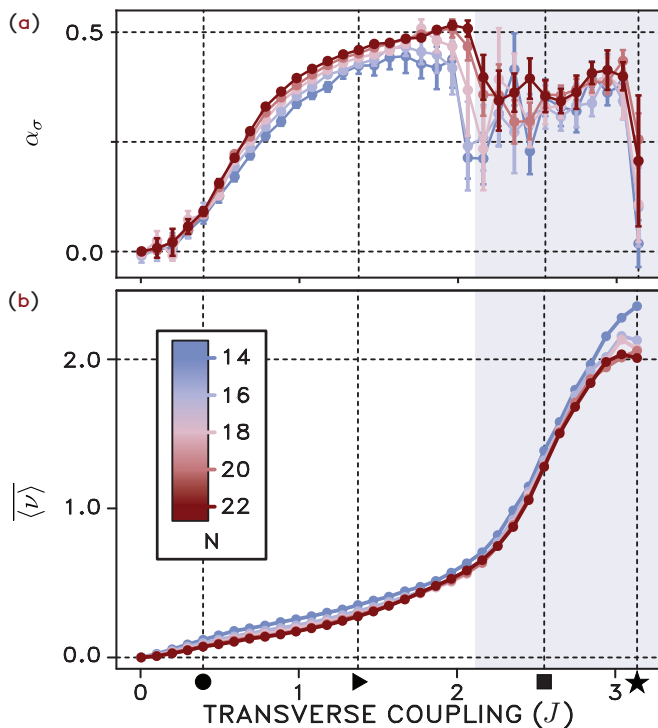

FIG. 6. In top panel (a) we see the diffusion coefficients α_σ extracted from Fig. 5(a). In the bottom, panel (b), reports the integrated speed for the on the time interval $t \in [0, T]$, where $T = N/2$.

sponds to a crossover from no transport at very small values of J, through an extended sub-diffusive regime, into diffusive transport. As J enters the swappy regime (highlighted as a shaded grey region), α_σ drops sharply and becomes less stable, as indicated by the wider error bars. This instability is attributed again to the wrapped Normal distribution being an inadequate model for $p_n(t)$

in this regime (see Fig. 5(c)). We later observe a similar instability in $\langle p_{\max}(t) \rangle$ in Fig. 7, wherein the transport exponent fluctuates drastically around unity. Close to the SWAP point $J \to \pi$, the results stabilize as α_σ rapidly approaches zero, indicating no spreading of the excitation.

The results in Fig. 5(b) indicates that the total distance traveled by the excitation increases as $J \to \pi$. It is thus instructive to define a time-averaged drift speed $\overline{\langle \nu \rangle}$ as:

$$\overline{\langle \nu \rangle} = \frac{1}{T} \int_0^T \langle \nu(t) \rangle \, dt \tag{17}$$

which spans from $\overline{\langle \nu \rangle} = 0$ in the localized phase to approximately $\overline{\langle \nu \rangle} \approx 2$ as $J \to \pi$, approaching the SWAP point. In this work, we take T to be the time needed for a SWAP circuit to return an excitation to its original position, $T = N/\nu_{\text{typ}}$, as discussed in App. A.

The results in Fig. 6(b) show smooth, stable behavior throughout the $J_z = \pi$ line. We observe that $\overline{\langle \nu \rangle}$ grows linearly across the localized and ergodic regimes, falling exactly to $\overline{\langle \nu \rangle} = 0$ in the fully-localized regime ($J \to 0$). Additionally $\overline{\langle \nu \rangle}$ increases dramatically up to a maximum value of $\overline{\langle \nu \rangle} = 2$ beyond the point $J \approx 2.1$ at which the transport exponent α_σ breaks down in Fig. 6(a). This behavior remains consistent across all system sizes N, but no clear crossover is visible and a more comprehensive finite-size scaling analysis is needed to extract specific critical values and exponents.

In Fig. 5(b), early-time drift is noticeable in both ergodic and swappy regimes but quickly stabilizes. A sharp rise in $\overline{\langle \nu \rangle}$ in the destabilized α_σ region (shaded gray in Fig. 6) suggests coherent late-time information transport. As N increases, we observe a small plateau at $\overline{\langle \nu \rangle} = 2$, consistent with App. A, implying that the swappy and
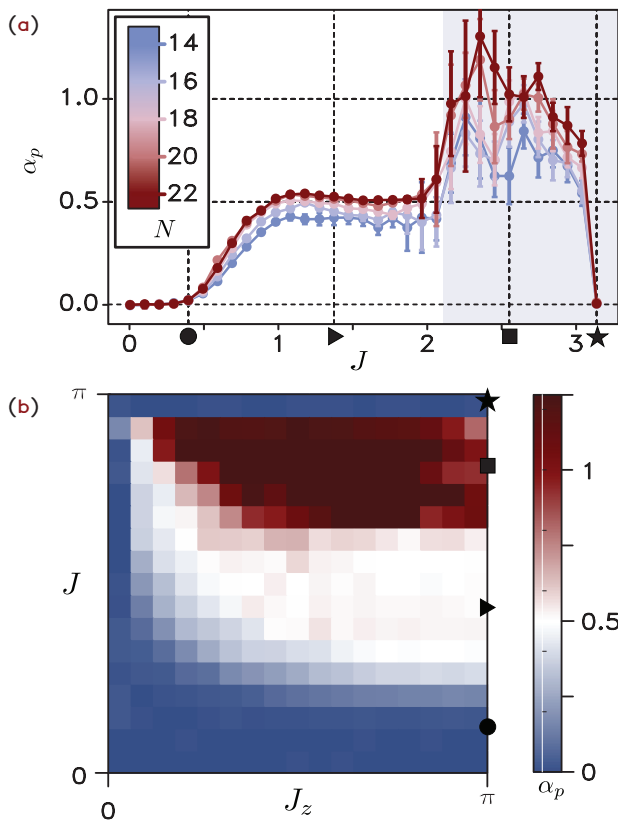
FIG. 7. Phase diagram of the exponent extracted from the decay of the $\langle p_{\max}(t) \rangle$, at $N = 20$ averaged over 30 trajectories. We can see a stable area where $\alpha_p \approx 1/2$ and a clear red area above it where the value of α_p also surpasses 1. Although this last area does not allow to probe transport coefficients it allows to identify where the swappy regime takes place.

near-SWAP regimes remain stable for large N, except at ultra-late times.

We analyze the exponent α_p derived from the peak value $\langle p_{\max}(t) \rangle \sim t^{-\alpha_p}$, using the same method applied for $\langle \sigma(t) \rangle$. As shown in Fig. 7(a), we find more robust and scale-sensitive results than those in Fig. 6(a). The plateaus at $\alpha_p \approx 0$ (full localization) and $\alpha_p \approx 1/2$ (diffusive transport) have stabilized, emerging clearly as scaling limits as N increases. Although results remain somewhat unstable as J approaches the swappy regime, a clearer structure is evident compared to Fig. 6(a). Larger system sizes N generally increase α_p in this region, indicating the onset of very rapid thermalization consistent with super-diffusive ($\alpha_p > 1/2$) transport exponents. At $J \to \pi$, α_p nearly vanishes, as expected, since no excitation spreading occurs in this limit.

Finally, we extract the transport exponent α_p from $\langle p_{\max}(t) \rangle \sim t^{\alpha_p}$ across the entire phase diagram to assess the stability of all regimes away from the $J_z = \pi$ line (and thus the validity of our schematic intuition in Fig. 1). These results are shown for $N = 20$ in Fig. 7(b) wherein we identify the four regimes unambiguously: ($\bullet$) $\alpha_p \approx 0$ in the localized regime, ($\blacktriangleright$) $\alpha_p \approx 1/2$ in the er-

godic regime, ($\blacksquare$) $\alpha_p > 1/2$ in the swappy regime, and ($\bigstar$) $\alpha_p \approx 0$ in the near-SWAP regime as we approach the DU line. Fig. 7(b) also shows clear crossovers between these regimes. with the localized-ergodic crossover consistent with gap ratio results shown in Fig. 2(b). Surprisingly, away from $J_z = \pi$ we find exponents consistent with ballistic $\alpha_p \approx 1$ transport or super-ballistic $\alpha_p > 1$ transport; though the connection between the relaxation of local observables to true transport properties is tenuous, and the nature of transport via e.g. conductance measurements is a topic worth interrogating in future research. We remark further on these high exponents further in our heuristic discussion of the swappy regime in Sec. IV B 5.

5. Prethermalization and the swappy regime

These results collectively establish the existence of a swappy regime as a distinct feature unique to discrete many-body systems, and located between the ergodic regime and DU line. Here we interrogate the stability and nature of this regime.

Based on our previous results we expect that in the swappy and near-SWAP regimes the system will eventually fully thermalize at very late times. However, in this section we argue that these regimes are characterized by prethermal behavior, i.e., that the time needed for thermalization diverges as we approach the integrable SWAP point. To verify this interpretation of the swappy regime, we present (i) a numerical investigation of the time taken for the system to thermalize; and (ii) a potential mechanism driving the swappy regime.

First, (i) we numerically investigate thermalization timescales in the swappy regime by computing the time t_p needed for the quantity $\langle p_{\max}(t) \rangle$ to decay to a specified threshold value. This time t_σ will serve as an estimate of the thermalization timescale. Similarly, we compute the time t_p needed for the decay of the excitation $\langle p_{\max}(t) \rangle$ to reach a specified threshold value, which we expect to give similar results. We examine the behavior of the thermalization timescale as a function of the parameter $J' = \pi - J$, which represents the deviation of J from the integrable SWAP point at $J = \pi$, and at which we expect the thermalization time to diverge. Our numerical results are plotted in Fig. 8(a) and (b). We see that, as J' decreases to zero (i.e., as we approach the SWAP point) the thermalization times diverge as $t_p \propto (J')^{-2.6}$ and $t_\sigma \propto (J')^{-2.4}$. Both exhibit a power-law scaling with an exponent ≈ 2 that is expected generically for prethermalization due to proximity to an integrable point [50]. This implies the existence of an extended prethermal swappy regime. We note that the precise numerical values of the power-law exponents for the thermalization times are contingent on our ad-hoc choice of the threshold values for $\langle p_{\max}(t) \rangle$ and $\langle \sigma(t) \rangle$ that determine our thermalization condition. However, we have checked that the exponents are ≈ 2 for a broad

range of threshold values.

Finally, (ii) we suggest a potential mechanism for the prethermal behaviour in the swappy regime. We suggest that a potential mechanism for swappy behavior is the "fragmentation" of the initial excitation into local populations reminiscent of the on-site populations of particles undergoing (potentially directionally-biased) one-dimensional random walks; i.e. that the swappy regime is an essentially single-particle phenomenon. Our proposed mechanism is as follows: near the SWAP point, the effect of local unitaries $\hat{U}_{n,n+1}$ on the local magnetization s_n^z on site n is realized in two ways, (i) the exchange of most (p_n) of s_n^z to the $n+1$th site, and (ii) a remnant $(1-p_n)$ of s_n^z that is left behind on the original site n. Essentially, we can approximate the dynamics close to the SWAP point as a classical Markov chain realizing the evolution of populations according to a classical update rule such as: $s_{n+1}^z = (1-p_{n+1})s_{n+1}^z + p_n s_n^z$. For imperfect SWAP gates, $p_n < 1$, excitations recursively "split" as consecutive imperfect SWAP gates are applied. We can explicitly see this splitting behavior realized as a 'checkerboard' pattern in Fig. 3(c) and (to a lesser extent due to averaging) (g). As $J \to \pi$ this splitting behavior vanishes, as is seen in the near-SWAP regime of Fig. 3(d) and (h), and we retrieve perfect swap dynamics, even at late times. This proposed mechanism is exact for small perturbations J' away from the SWAP point along the diagonal $J = J_z = \pi - J'$, wherein (neglecting the local disorder terms, and global phases) the local unitary can be decomposed as:

$$\hat{U}_{n,n+1} = e^{-i(\pi-J')\hat{\mathbf{S}}_n \cdot \hat{\mathbf{S}}_{n+1}} \tag{18}$$

$$= \widehat{\mathrm{SWAP}}_{n,n+1} \left[\mathbb{I} + iJ'\hat{\mathbf{S}}_n \cdot \hat{\mathbf{S}}_{n+1} \right] + \mathcal{O}(J'^2) \tag{19}$$

$$= \left(1 - \frac{iJ'}{4}\right) \widehat{\mathrm{SWAP}}_{n,n+1} + i\frac{J'}{2}\mathbb{I} + \mathcal{O}(J'^2) \tag{20}$$

such that, after application to some test state,

$$\hat{U}_{n,n+1}|\psi\rangle \approx \frac{1}{\sqrt{\mathcal{N}}} \left[\left(1 - \frac{iJ'}{4}\right)|\widetilde{\psi}\rangle + i\frac{J'}{2}|\psi\rangle \right] \tag{21}$$

where $\widehat{\mathrm{SWAP}}|\psi\rangle = |\widetilde{\psi}\rangle$, and $\mathcal{N}$ is some appropriate normalization constant. This brings the Markov chain description of short-time dynamics close to the SWAP point $J' = 0$ discussed above into sharp clarity; with the probabilities p_n determined by the value of J'. As J' increases, the $\mathcal{O}(J')$ term in Eq. (20) yields noticeable effects on the dynamics at earlier times. We interrogate these effects here by extracting prethermal timescales, where we find numerical evidence supporting our above discussion. However, a detailed semi-classical analysis of the swappy regime according to this intuition, and its connection to the sudden thermalization seen in Fig. 3(c) and (g), is beyond the scope of this paper, and is deferred to future study.
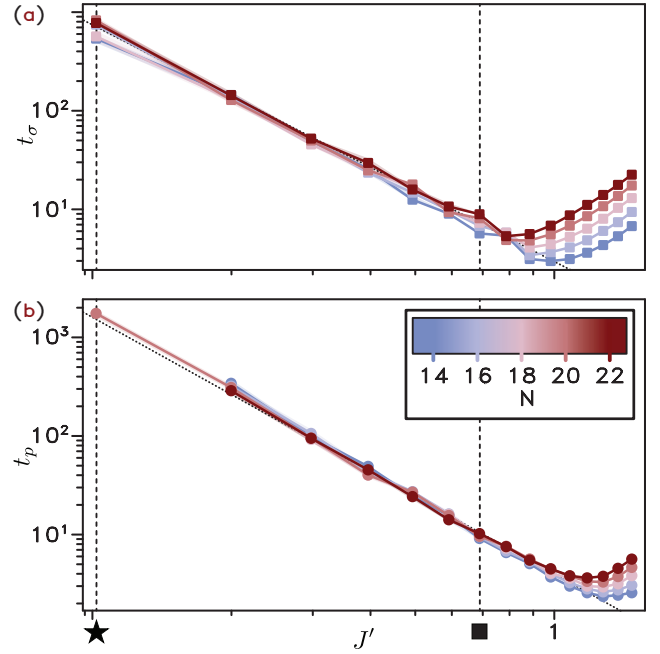

FIG. 8. Prethermal scaling near the SWAP point. Values are extracted from $\sigma(t)$, as $t_\sigma = \inf\{t \mid \sigma(t) > N/30 + 1.25\}$ (panel (a)), and from $p_{\max}(t)$, as $t_p = \inf\{t \mid p_{\max}(t) < 2.6/N\}$ (panel (b)). The dotted lines are $t \propto (J')^{-2.4}$ and $t \propto (J')^{-2.6}$, respectively.

V. CONCLUSIONS

Our results address transport across various phases of a highly generic $U(1)$-symmetric disordered Floquet model, revealing a wide array of phenomenological behaviors. This includes more conventional localized and ergodic regimes, exhibiting sub-diffusive and diffusive transport respectively; and the existence of a "swappy" regime unique to discrete-time quantum systems, in which excitations propagate ballistically. To enable this investigation, we study the model from both static and dynamic perspectives, by focusing in the zero magnetization subsector. The former is pursued by means of POLFED, adapted to work in a given magnetization subsector by applying the unitary gate-by-gate. We have developed and deployed the first circular moment (see Fig. 4 and discussion thereof): a quantity defined for periodic systems which directly encodes their transport properties, and which maps their aggregated dynamics onto simple yet striking two-dimensional diagrams. This quantity provides a visual and intuitive way to understand transport across different regimes in periodic systems; and, as it is singularly composed of local Z-basis expectation values, is highly amenable to experimental implementation; paving the way for the near-future experimental analysis of transport in digital matter. Of this quantity we analyze the decay, connected to the spread of the initial excitation, and speed of its phase, from which we define a notion of drift. Our drift might be linked

to the concept of entanglement speed [73, 74], particularly in the near-SWAP regime where it aligns with the characteristics of entanglement speed in DU circuits.

Our results, taken in concert, demonstrate the existence of a swappy regime which is (i) distinct: exhibiting a clear ergodic-swappy crossover in the vicinity of $J \sim 2.1$ for all investigated dynamical quantities of Sec. IV B, (ii) dynamical: as it is absent in the static analyses of Sec. IV A, (iii) prethermal: exhibiting a failure to thermalize until late timescales which grow as a power law in $t \sim (\pi - J)^{-2}$ (see Sec. IV B 5), (iv) stable to perturbations in J and J_z (see Fig. 7(b) and discussion thereof), (v) stable as a function of system size (see e.g. Fig. 6 and Fig. 8), and (vi) unique to discrete-time Floquet systems, appearing in the vicinity of the DU line at $J = \pi$, which has no counterpart in continuous models. We also provide a rough outline of a potential semi-classical mecha-

nism underlying this regime; though we defer a detailed analysis of this mechanism to future study.

VI. ACKNOWLEDGMENTS

[1] H. F. Trotter, Proceedings of the American Mathematical Society **10**, 545–551 (1959).

[2] M. Suzuki, Physics Letters A **146**, 319–323 (1990).

[3] D. W. Berry, A. M. Childs, R. Cleve, R. Kothari, and R. D. Somma, Phys. Rev. Lett. **114**, 090502 (2015).

[4] G. H. Low and I. L. Chuang, Phys. Rev. Lett. **118**, 010501 (2017).

[5] E. Campbell, Phys. Rev. Lett. **123**, 070503 (2019).

[6] S. Barison, F. Vicentini, and G. Carleo, Quantum **5**, 512 (2021).

[7] B. Fauseweh, Nature Communications **15** (2024), 10.1038/s41467-024-46402-9.

[8] J. Richter and A. Pal, Phys. Rev. Lett. **126**, 230501 (2021).

[9] A. Summer, C. Chiaracane, M. T. Mitchison, and J. Goold, Physical Review Research **6**, 013106 (2024).

[10] N. Yoshioka, M. Amico, W. Kirby, P. Jurcevic, A. Dutt, B. Fuller, S. Garion, H. Haas, I. Hamamura, A. Ivrii, R. Majumdar, Z. Minev, M. Motta, B. Pokharel, P. Rivero, K. Sharma, C. J. Wood, A. Javadi-Abhari, and A. Mezzacapo, "Diagonalization of large many-body hamiltonians on a quantum processor," (2024), arXiv:2407.14431.

[11] N. Keenan, N. F. Robertson, T. Murphy, S. Zhuk, and J. Goold, npj Quantum Information **9**, 72 (2023).

[12] X. Mi and A. A. e. a. Michailidis, Science **383**, 1332–1337 (2024).

[13] G. Q. AI and Collaborators, "Observation of disorder-free localization and efficient disorder averaging on a quantum processor," (2024), arXiv:2410.06557.

[14] L. E. Fischer, M. Leahy, A. Eddins, N. Keenan, D. Ferracin, M. A. C. Rossi, Y. Kim, A. He, F. Pietracaprina, B. Sokolov, S. Dooley, Z. Zimborás, F. Tacchino, S. Maniscalco, J. Goold, G. García-Pérez, I. Tavernelli, A. Kandala, and S. N. Filippov, "Dynamical simulations of many-body quantum chaos on a quantum computer," (2024), arXiv:2411.00765.

[15] V. Khemani, A. Lazarides, R. Moessner, and S. L. Sondhi, Phys. Rev. Lett. **116**, 250401 (2016).

[16] X. Mi, M. Ippoliti, and C. e. a. Quintana, Nature **601**, 531–536 (2021).

[17] B. Skinner, J. Ruhman, and A. Nahum, Phys. Rev. X **9**, 031009 (2019).

[18] X. Turkeshi, A. Biella, R. Fazio, M. Dalmonte, and M. Schiró, Phys. Rev. B **103**, 224210 (2021).

[19] C. Noel, P. Niroula, D. Zhu, A. Risinger, L. Egan, D. Biswas, M. Cetina, A. V. Gorshkov, M. J. Gullans, D. A. Huse, and C. Monroe, Nature Physics **18**, 760–764 (2022).

[20] L. Logarić, S. Dooley, S. Pappalardi, and J. Goold, Phys. Rev. Lett. **132**, 010401 (2024).

[21] B. Andrade, U. Bhattacharya, R. W. Chhajlany, T. Graß, and M. Lewenstein, Phys. Rev. A **109**, 052602 (2024).

[22] S. Moudgalya and O. I. Motrunich, Phys. Rev. X **12**, 011050 (2022).

[23] Y. Han, X. Chen, and E. Lake, "Exponentially slow thermalization and the robustness of hilbert space fragmentation," (2024), arXiv:2401.11294.

[24] L. Logarić, J. Goold, and S. Dooley, "Hilbert subspace ergodicity," (2024), in preparation.

[25] L. Piroli and J. I. Cirac, Phys. Rev. Lett. **125**, 190402 (2020).

[26] M. Vanicat, L. Zadnik, and T. c. v. Prosen, Phys. Rev. Lett. **121**, 030606 (2018).

[27] M. Ljubotina, L. Zadnik, and T. Prosen, Phys. Rev. Lett. **122**, 150605 (2019).

[28] M. Ljubotina, M. Žnidarič, and T. Prosen, Phys. Rev. Lett. **122**, 210602 (2019).

[29] H. Bethe, Zeitschrift fur Physik **71**, 205–226 (1931).

[30] B. Bertini, M. Collura, J. De Nardis, and M. Fagotti, Phys. Rev. Lett. **117**, 207201 (2016).

[31] M. Žnidarič, A. Scardicchio, and V. K. Varma, Phys. Rev. Lett. **117**, 040601 (2016).

[32] T. c. v. Prosen, Phys. Rev. Lett. **106**, 217206 (2011).

[33] A. Pal and D. A. Huse, Phys. Rev. B **82**, 174411 (2010).

[34] D. J. Luitz, N. Laflorencie, and F. Alet, Phys. Rev. B **91**, 081103 (2015).

[35] D. A. Abanin, E. Altman, I. Bloch, and M. Serbyn, Rev. Mod. Phys. **91**, 021001 (2019).

[36] A. Nico-Katz, A. Bayat, and S. Bose, Phys. Rev. Res. 4, 033070 (2022).

[37] A. Nico-Katz, A. Bayat, and S. Bose, Phys. Rev. B 105, 205133 (2022).

[38] M. Serbyn, Z. Papić, and D. A. Abanin, Phys. Rev. B 90, 174302 (2014).

[39] M. Serbyn, Z. Papić, and D. A. Abanin, Phys. Rev. X 5, 041047 (2015).

[40] V. Khemani, D. N. Sheng, and D. A. Huse, Phys. Rev. Lett. 119, 075702 (2017).

[41] D. J. Luitz, I. M. Khaymovich, and Y. B. Lev, SciPost Phys. Core 2, 006 (2020).

[42] A. Nico-Katz and S. Bose, Phys. Rev. Res. 5, 013041 (2023).

[43] J. Colbois, F. Alet, and N. Laflorencie, Phys. Rev. Lett. 133, 116502 (2024).

[44] P. Sierant, M. Lewenstein, A. Scardicchio, and J. Zakrzewski, Phys. Rev. B 107, 115132 (2023).

[45] S. Gopalakrishnan and A. Lamacraft, Phys. Rev. B 100, 064309 (2019).

[46] B. Bertini, P. Kos, and T. Prosen, Phys. Rev. Lett. 123, 210601 (2019).

[47] R. Peierls, Zeitschrift fur Physik 80, 763–791 (1933).

[48] Y. Bar Lev, G. Cohen, and D. R. Reichman, Phys. Rev. Lett. 114, 100601 (2015).

[49] C. Sünderhauf, D. Pérez-García, D. A. Huse, N. Schuch, and J. I. Cirac, Phys. Rev. B 98, 134204 (2018).

[50] A. Morningstar, L. Colmenarez, V. Khemani, D. J. Luitz, and D. A. Huse, Phys. Rev. B 105, 174205 (2022).

[51] D. Hahn and L. Colmenarez, "Localization and integrability breaking in weakly interacting Floquet circuits," (2023), arXiv:2311.02197 [cond-mat.stat-mech].

[52] O. Shtanko, D. S. Wang, H. Zhang, N. Harle, A. Seif, R. Movassagh, and Z. Minev, "Uncovering local integrability in quantum many-body dynamics," (2023), arXiv:2307.07552 [quant-ph].

[53] D. M. Long, P. J. D. Crowley, V. Khemani, and A. Chandran, Phys. Rev. Lett. 131, 106301 (2023).

[54] V. Khemani, A. Vishwanath, and D. A. Huse, Physical Review X 8, 031057 (2018).

[55] T. Rakovszky, F. Pollmann, and C. W. von Keyserlingk, Phys. Rev. X 8, 031058 (2018).

[56] C. Jonay, J. F. Rodriguez-Nieva, and V. Khemani, Phys. Rev. B 109, 024311 (2024).

[57] J. Zhang, J. Vala, S. Sastry, and K. B. Whaley, Phys. Rev. A 67, 042313 (2003).

[58] P. Sierant, M. Lewenstein, A. Scardicchio, L. Vidmar, and J. Zakrzewski, "Many-Body Localization in the Age of Classical Computing," (2024), 2403.07111 [cond-mat, physics:quant-ph].

[59] R. K. Panda, A. Scardicchio, M. Schulz, S. R. Taylor, and M. Žnidarič, Europhysics Letters 128, 67003 (2020).

[60] D. N. Page, Phys. Rev. Lett. 71, 1291 (1993).

[61] L. D'Alessio and M. Rigol, Phys. Rev. X 4, 041048 (2014).

[62] Y. Y. Atas, E. Bogomolny, O. Giraud, and G. Roux, Phys. Rev. Lett. 110, 084101 (2013).

[63] T. L. M. Lezama, S. Bera, and J. H. Bardarson, Phys. Rev. B 99, 161106 (2019).

[64] R. Nandkishore and D. A. Huse, Annual Review of Condensed Matter Physics 6, 15–38 (2015).

[65] F. Alet and N. Laflorencie, Comptes Rendus. Physique 19, 498–525 (2018).

[66] P. Sierant and J. Zakrzewski, Phys. Rev. B 105, 224203 (2022).

[67] R. Steinigeweg and J. Gemmer, Phys. Rev. B 80, 184402 (2009).

[68] B. Bertini, F. Heidrich-Meisner, C. Karrasch, T. Prosen, R. Steinigeweg, and M. Žnidarič, Rev. Mod. Phys. 93, 025003 (2021).

[69] M. V. Berry, Journal of Physics A: Mathematical and General 10, 2083 (1977).

[70] S. Roy, Y. B. Lev, and D. J. Luitz, Phys. Rev. B 98, 060201 (2018).

[71] In practice, we find it more effective to evaluate coherent transport via an instantaneous drift *speed*, $\nu(t)$, derived from a modified mean parameter, $\tilde{\mu}(t)$, as follows:

$$\nu(t) = \left| \frac{d\tilde{\mu}(t)}{dt} \right| = \mathrm{Arg}\left[\sum_n p_n(t) e^{i|\theta_n|} \right], \qquad (22)$$

where this modification restricts $|\theta_n| \in [0, \pi]$ and addresses discontinuities in $\mu(t)$ that arise as excitations cross the boundary's coordinate discontinuity. Numerical evidence supporting the presence of these discontinuities is presented in Fig. 4.

[72] To refine α_σ, we perform 25 iterative fits, slightly varying the time window. Each time window is perturbed by a normally distributed factor with mean 1 and $\sigma = 0.2$. For each fit, $\langle \sigma(t) \rangle$ is computed from a third of the trajectories (randomly sampled). We then take the logarithm of $\langle \sigma(t) \rangle$ and t, fitting the data to $b \ln t + c$, with α_σ estimated as the mean of the b coefficients across all runs. This method minimizes sensitivity to both the time window choice and the average $\langle \sigma \rangle$ value. The same procedure is applied to $p_{\max}$ to estimate α_p.

[73] T. Zhou and A. W. Harrow, Phys. Rev. B 106, L201104 (2022).

[74] M. A. Rampp, S. A. Rather, and P. W. Claeys, "Geometric constructions of generalized dual-unitary circuits from biunitarity," (2024), arXiv:2411.07783.

[75] D. J. Luitz, SciPost Phys. 11, 021 (2021).

[76] J. Skilling, "The axioms of maximum entropy," in *Maximum-Entropy and Bayesian Methods in Science and Engineering: Foundations*, edited by G. J. Erickson and C. R. Smith (Springer Netherlands, Dordrecht, 1988) pp. 173–187.

[77] A. Weiße, G. Wellein, A. Alvermann, and H. Fehske, Rev. Mod. Phys. 78, 275 (2006).
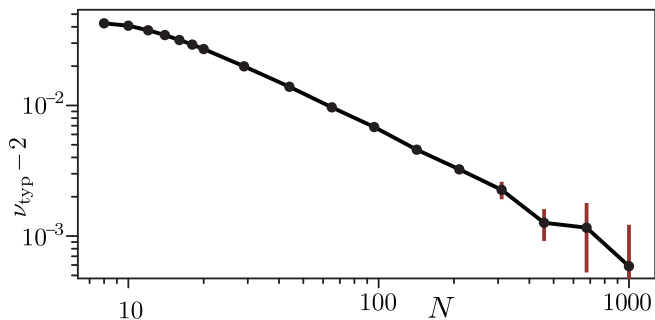
FIG. 9. Difference of typical drift and BW drift for different values of N. For $N \leq 10$ the value is exact, by studying all the $N!$ permutations. We sample 10^7 trajectories for $N \leq 20$, then $10^7/3$ for $N < 50$, 10^6 for $N < 250$, $10^6/3$ for $N < 500$, otherwise 10^5.

Appendix A: Typical drift

The random permutation of gates enables the restoration of translational invariance by averaging over different permutations. This averaged circuit will have some averaged properties such as an average drift. To analyze this, we can consider a circuit composed exclusively of generalized SWAP gates (i.e., $J = \pi$, as from Eq. (3)) and investigate the resultant circuit after averaging over these permutations. Let us focus on the scenario with same initial state as Eq. (7), namely with an excitation located at the middle site of the chain. We can define the drift as an effective speed, calculated as the number of sites traversed to return to the initial one (N sites) divided by a time. This time corresponds to the number of gates applied, normalized over N (i.e., the number of gates per Floquet cycle).

By studying this, we observe that most efficient circuits for returning the excitation to its starting site are the two staircase circuits that begin with the gate $\hat{U}_{N/2,N/2+1}$ (or $\hat{U}_{N/2-1,N/2}$), employing the permutation $P : i \mapsto N/2 - 1 + i$ (or $P : i \mapsto N/2 - i$). These configurations yield a drift value of $\nu = N$. Conversely, when the staircase geometry is reversed, using permutations like $P : i \mapsto N/2 - 2 + i$ or $P : i \mapsto N/2 + 1 - i$, the drift value drops to $N^2/(N^2 - 2N + 2)$, which tends to 1 as N grows.

Calculating the drift precisely involves evaluating all $N!$ possible permutations, and we could not express this in a closed form. However, by sampling a large number of permutations, we can accurately estimate the average drift very accurately.

Our findings reveal that for $N \geq 8$, the average drift decreases monotonically towards 2, corresponding to the value associated with brickwork circuits. Since brickwork circuits are the most commonly obtained configuration under random P, we define this average drift as the typical drift, denoted by ν_{typ}. For instance, at $N = 20$, after sampling 10^7 trajectories, the average drift was found to be $\nu_{\mathrm{typ}} \approx 2.027(6)$. This power-law-like trend approach-

ing 2 is presented in Fig. 9.

Appendix B: Numerical methods

The entanglement entropy values we compute are derived from the mean of $\min(d/10, 750)$ eigenvectors. To acquire these eigenvectors, we employ polynomial filtered diagonalization (POLFED) [75], a spectral transformation akin to the shift-invert method, tailored for unitary matrices. The Floquet operator $\hat{\mathbb{U}}$ is redefined as the operator

$$\hat{\mathbb{K}} = \sum_{k=0}^{K} e^{-ik\phi_{\mathrm{tgt}}} \hat{\mathbb{U}}^k \tag{B1}$$

This new operator is non-unitary yet retains the eigenvectors of the original Floquet operator. Moreover, the eigenphases of $\hat{\mathbb{U}}$ within the interval delimited by $(\phi_{\mathrm{tgt}} \pm 2\pi/K)$ are now transformed such that their absolute values exceed 1, while the others are less than 1. This enhances the convergence properties of the Arnoldi method, which we employ to derive the eigenphases and eigenvectors of $\hat{\mathbb{U}}$. In this study, we consistently selected $\phi_{\mathrm{tgt}} = 0$. For the parameter K, we adopted the recommendation from Ref. [75], setting K to $0.4 \, d/\min(d/10, 750)$.

The numerical method we developed circumvents the need to construct the entire $\hat{\mathbb{U}}$ matrix. Instead, we apply each gate directly to the state vector, leveraging the fact that both static and dynamic analyzes necessitate the application of the Floquet operator to a state. This allows the memory cost of diagonalising $\hat{\mathbb{U}}$ to be $O(d)$ and the number of operations to be $O(Ld)$, similar to what pointed out in Ref. [50].

Our approach involves recording the action of a gate on the first two spins of a state $|\psi\rangle$. If a gate acts on spins a and $a+1$, we shift the system by $-a$ sites, apply the gate to the first two spins, and then shift the system back to its original configuration.

To implement this, we require two key components. First, we must determine the value of the first two spins for each element of $|\psi\rangle$. The state is represented as a d-vector:

$$|\psi\rangle = \sum_i c_i |i\rangle \tag{B2}$$

where the i-th element corresponds to the $|i\rangle$ state. Hence, we need to identify which segments of the d-vector have the first and second spins up, namely which of the c_i are associated with a $|i\rangle$ with first and second spin up.

The second ingredient involves the transformation $f_{(1)}$, which maps a state from sites $0, \ldots, N-1$ to the corresponding state on sites $N-1, 0, \ldots, N-2$. By recursively applying $f_{(1)}$, we can achieve the required

shift, i.e., $f_{(a)} = f_{(1)}^a$. This strategy offers a significant memory advantage, as it only necessitates storing vectors of size d Although this comes with a cost in the number of operations —each gate of $\hat{\mathbb{U}}$ or $\hat{\mathbb{K}}$ must be applied sequentially— the memory efficiency of this method allows for better parallel computation of multiple trajectories, which is crucial for disorder averaging.

To compute the entropy, we can reduce the computation to different magnetization sub-sectors. Specifically, the entanglement entropy, given by Eq. (4), can be calculated by reshaping the state $|\psi\rangle$ into a $d_A \times d_B$ matrix and extracting its Schmidt coefficients s_i via Singular Value Decomposition (SVD). The von Neumann entropy of $|\psi\rangle$ is then

$$S(|\psi\rangle) = -\sum_i s_i^2 \ln s_i^2. \tag{B3}$$

Among these steps, the SVD is the most computationally intensive. However, we can exploit the structure of the system further. The space d_A can be decomposed as

$$\mathcal{H}_A^{(M)} = \bigoplus_{M_A=-N/2}^{N/2} \mathcal{H}_{A,(M_A)}^{(M)}. \tag{B4}$$

Given that $|\psi\rangle$ resides in $\mathcal{H}^{(M)}$ with $M = 0$, if the A part has magnetization M_A, the B part will have magnetization $M_B = M - M_A$. Consequently, for each M_A value we can isolate the component of $|\psi\rangle$ in $\mathcal{H}_{A,(M_A)}^{(M)}$, reshape it into a $d_{A,(M_A)}^{(M)} \times d_{B,(M_B)}^{(M)}$ matrix, and compute the SVD on this smaller matrix. In other terms, we split the zero-magnetization sub-sector as

$$\mathcal{H}^{(M)} = \bigoplus_{M_A=-N/2}^{N/2} \mathcal{H}_{A,(M_A)}^{(M)} \otimes \mathcal{H}_{B,(M-M_A)}^{(M)}. \tag{B5}$$

The total entanglement entropy of the state is then given by

$$S(|\psi\rangle) = -\sum_{M_A} \sum_{i \in M_A} s_i^2 \ln s_i^2. \tag{B6}$$

By sidestepping the full d-state vector's SVD, the process of extracting entanglement entropy becomes more efficient, and significantly more manageable.

Appendix C: Reduction of four phases to two plus the Peierls phase in $U(1)$-symmetric gates

Although the gate $\hat{U}_{n,n+1}$, defined in Eq. (1), remains the most general $U(1)$-symmetric gate, we preferred, for the purposes of our numerical method, to precompute $\hat{H}_{n,n+1}$ without phases and then add them individually gate by gate.

The initial gate we employ is

$$\begin{aligned}
\hat{V}_{n,n+1} =& e^{-i\theta_1^{(n)}/2\hat{\sigma}_n^z} e^{-i\theta_2^{(n)}/2\hat{\sigma}_{n+1}^z} \\
& e^{-iJ/4\,\hat{\sigma}_n^x\hat{\sigma}_{n+1}^x} e^{-iJ/4\,\hat{\sigma}_n^y\hat{\sigma}_{n+1}^y} e^{-iJ_z/4\,\hat{\sigma}_n^z\hat{\sigma}_{n+1}^z} \\
& e^{-i\theta_3^{(n)}/2\hat{\sigma}_n^z} e^{-i\theta_4^{(n)}/2\hat{\sigma}_{n+1}^z}
\end{aligned} \tag{C1}$$

where the Pauli operators are swapped out for spin operators:

$$\hat{\sigma}^z = \hat{S}^z/2 \qquad \hat{\sigma}^\pm = \hat{S}^\pm. \tag{C2}$$
$$\tag{C3}$$

This substitution yields the expression:

$$\begin{aligned}
\hat{V}_{n,n+1} =& e^{-iJ_z\,\hat{S}_n^z\hat{S}_{n+1}^z} e^{-i\theta_1^{(n)}\hat{S}_n^z} e^{-i\theta_2^{(n)}\hat{S}_{n+1}^z} \\
& e^{-iJ/2\left(\hat{S}_n^+\hat{S}_{n+1}^- + \hat{S}_n^-\hat{S}_{n+1}^+\right)} \\
& e^{-i\theta_3^{(n)}\hat{S}_n^z} e^{-i\theta_4^{(n)}\hat{S}_{n+1}^z}.
\end{aligned} \tag{C4}$$

Due to the commutativity of the two-body terms, this simplifies to:

$$\begin{aligned}
\hat{V}_{n,n+1} =& e^{-iJ_z\,\hat{S}_n^z\hat{S}_{n+1}^z} e^{-i\theta_1^{(n)}\hat{S}_n^z - i\theta_2^{(n)}\hat{S}_{n+1}^z} \\
& e^{-iJ/2\,(\hat{S}_n^+\hat{S}_{n+1}^- + \hat{S}_n^-\hat{S}_{n+1}^+)} \\
& e^{i\theta_1^{(n)}\hat{S}_n^z + i\theta_2^{(n)}\hat{S}_{n+1}^z} \\
& e^{-i(\theta_1^{(n)}+\theta_3^{(n)})\hat{S}_n^z - i(\theta_2^{(n)}+\theta_4^{(n)})\hat{S}_{n+1}^z}
\end{aligned} \tag{C5}$$

where the $\hat{S}^\pm$ operators, flanked by opposite phases, generate the Peierls phase, condensing the notation into:

$$\begin{aligned}
\hat{V}_{n,n+1} =& e^{-iJ_z\,\hat{S}_n^z\hat{S}_{n+1}^z} \\
& e^{-iJ/2\left(\hat{S}_n^+\hat{S}_{n+1}^- e^{i(\theta_1^{(n)}-\theta_2^{(n)})} + \hat{S}_n^-\hat{S}_{n+1}^+ e^{-i(\theta_1^{(n)}-\theta_2^{(n)})}\right)} \\
& e^{-i(\theta_1^{(n)}+\theta_3^{(n)})\hat{S}_n^z - i(\theta_2^{(n)}+\theta_4^{(n)})\hat{S}_{n+1}^z} \\
=& \hat{U}_{n,n+1}
\end{aligned} \tag{C6}$$

where $\hat{U}_{n,n+1}$'s parameters are:

$$\phi_n = \theta_1^{(n)} - \theta_2^{(n)}, \quad \alpha_n = \theta_1^{(n)} + \theta_3^{(n)}, \text{ and } \beta_n = \theta_2^{(n)} + \theta_4^{(n)}. \tag{C7}$$

Owing to the 2π periodicity of ϕ_n, α_n, and β_n, the sum or difference of the uniformly distributed $\theta_k^{(n)}$ within $[-\pi, \pi]$ ensures that the resulting parameters are uniformly distributed in $[-\pi, \pi]$ as well.

This eventually proves that the black gates of Fig. 1(a) can be decomposed either as Eq. (1) or Eq. (C1):

$$\blacksquare = \blacksquare \quad = \quad \blacksquare \tag{C8}$$

Appendix D: Discretized Wrapped Normal distribution

As discussed in Sec. IV B 2, to quantify the rate of spreading, we compare the distribution of $p_n(t)$ with a
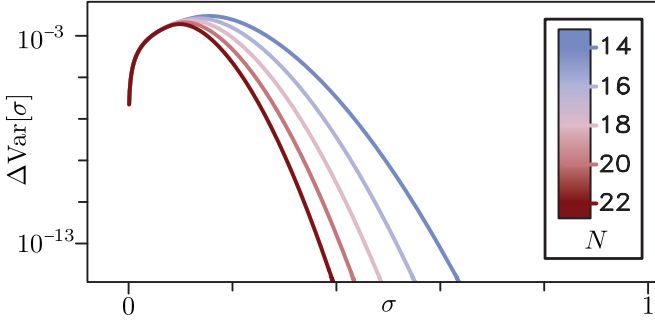
FIG. 10. Difference between the circular variance of discrete Wrapped Normal distributions compared to the continuous one. $\Delta \mathrm{Var}[\sigma]$ is defined as difference between continuous and discrete wrapped normal distribution.
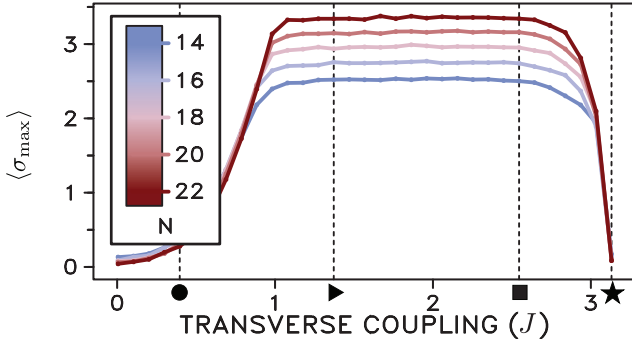

FIG. 11. Maximal value for the σ function for different system sizes and different J, along the $J_z = \pi$ line. We can notice how the curves seems to be estensive and so grow linearly with N.

wrapped Normal distribution. Since the wrapped Normal distribution has a continuous support, a more rigorous approach might be to discretize it. This discrete version of the wrapped Normal distribution would be defined as:

$$\tilde{q}_n(\sigma) = \sum_{k=-\infty}^{\infty} e^{-(\theta_n + 2\pi k)^2 / 2\sigma^2}, \qquad \text{(D1)}$$

with the normalized form given by

$$q_n(\sigma) = \frac{\tilde{q}_n(\sigma)}{\sum_n \tilde{q}_n(\sigma)}, \qquad \text{(D2)}$$

which introduces a more complex procedure for extracting σ, as there is no closed-form relationship between σ and $Var[\sigma]$. However, for already small values of N, the differences between the continuous and discrete distributions are minimal, and the added complexity does not significantly improve accuracy. In Fig. 10, we compare the variances of the continuous and discrete wrapped Normal distributions for different values of N. Our results indicate that, given the number of qubits in our simulations, the two distributions closely align, showing that the continuous approximation is sufficiently accurate.

Appendix E: Finite size scaling of saturation values of the spread parameter

In Sec. IV B 4 of the main text, we observed a distinct plateau in the late-time behavior of $\langle \sigma(t) \rangle$ as systems reach thermalization. This observation might seem counterintuitive, given that in a fully thermalized state, we would expect a uniform distribution with $|R(t)| \to 0$, implying $\sigma(t) \to \infty$ according to Eq. (13).

Here, we provide straightforward numerical evidence indicating that this plateau is a finite-size effect. Possible explanations for this effect include: (a) the wrapped Normal distribution only accurately represents $p_n(t)$ in the continuum limit $N \to \infty$, or (b) finite-dimensional systems lack the ability to fully self-thermalize. In Fig. 11, we display the maximum value of σ over the first $T = 1000$ time steps for various values of N. For values of J where the system thermalizes within this timeframe, $\langle \sigma_{\max} \rangle$ reaches a plateau that grows steadily with N.

Appendix F: Expanded Transport

Transport coefficients and exponents in many-body physics are typically derived from linear response theory [68]. In this Appendix we briefly review how the magnetization profile $M_n(t)$ for our particular choice of the initial random state $\hat{P}_{N/2}^{\uparrow} |\psi_{\mathrm{rand}}\rangle$, an in particular the resulting semiprobability $p_n(t)$, corresponds to the two-point correlation function of the spin z-operator $\hat{S}_n^z$. We divide our discussion into three steps. First, we illustrate how the spin profile of our initial state aligns with the correlation function of $\hat{S}_n^z$ within the complete Hilbert space. Second, we demonstrate how this can be tailored to the M-sub-sector. Finally, we connect this framework to typical random states, thereby fully linking our discussion to the definition of $M_n(t)$ of Sec. IV B 1.

1. Dynamical correlation function in the full Hilbert space

These coefficients are extracted from spatiotemporal correlations, which, in systems that conserve the total spin component $\hat{S}_{\mathrm{tot}}^z$, are defined as follows:

$$C_{n,n'}(t) = \mathrm{Tr}[\hat{S}_n^z(t) \hat{S}_{n'}^z]. \qquad \text{(F1)}$$

First we observe that the unpropagated spin operator can be decomposed as:

$$\hat{S}_{n'}^z = \hat{\mathbb{1}}_2^{\otimes N-1} \otimes \left(|\uparrow\rangle\langle\uparrow| - \hat{\mathbb{1}}_2/2 \right)_{n'} \qquad \text{(F2)}$$

$$= \hat{P}_{n'}^{\uparrow} - \hat{\mathbb{1}}_2^{\otimes N}/2 \qquad \text{(F3)}$$

where $\hat{\mathbb{1}}_2$ is the local two-dimensional identity, the subscript n' denotes which local Hilbert space the relevant local spin-z operator must be inserted into, and where the

projector $\hat{P}_{n'}^{\uparrow} = \hat{\mathbb{1}}_2^{\otimes N-1} \otimes |\uparrow\rangle\langle\uparrow|_{n'}$ projects the n'-th site onto the spin-up state. Direct substitution of Eq. (F3) into the correlation function yields

$$C_{n,n'}(t) = \text{Tr}\left[\hat{S}_n^z(t)\hat{P}_{n'}^{\uparrow}\right] - \text{Tr}[\hat{S}_n^z(t)]/2. \quad \text{(F4)}$$

wherein the second term reduces to zero by simple observance that spin operators are traceless $\text{Tr}[\hat{S}_n^z(t)] = 0$. The first term intuitively corresponds to the simple expectation value of the spin-z operator on the n-th site at time t, conditioned on the initial state being a maximally mixed state with the n'-th site projected into the spin-up state.

This intuition becomes even more developed when one considers the stochastic trace estimation approach to actual numerical computation of Eq. (F4). In practice, explicit calculation of the trace is computationally expensive, with a number of operations that naïvely scales as D^2 (where D is the dimensionality of the total system). It is therefore commonly computed stochastically [76, 77]:

$$C_{n,n'}(t) \simeq \frac{1}{R}\sum_{r=1}^{R}\langle\psi_r|\hat{S}_n^z(t)\hat{P}_{n'}^{\uparrow}|\psi_r\rangle. \quad \text{(F5)}$$

where $|\psi_r\rangle$ are random states, generated following the method of [77]. The accuracy of this approximation follows central limiting behavior, scaling as $\mathcal{O}(1/\sqrt{RD})$; thus we can set $R = 1$ and retrieve sufficiently accurate results by taking large system sizes $D = 2^N$ [9]. This approach replaces the stochastic average with the expectation value evaluating using single 'typical' state $|\psi_{\text{typ}}\rangle$ (i.e., a single realization of $|\psi_r\rangle$). By absorption of the identities into the state vector $|\psi_r\rangle$, exploitation of the projector property $(\hat{P}_{n'}^{\uparrow})^2 = \hat{P}_{n'}^{\uparrow}$, the cyclicity of the trace, and by moving out of the Heisenberg picture, we arrive at the following form for the correlation function:

$$C_{n,n'}(t) \simeq \langle\psi_{\text{typ}}|\hat{P}_{n'}^{\uparrow}\hat{\mathbb{U}}^{\dagger t}\hat{S}_n^z\hat{\mathbb{U}}^t\hat{P}_{n'}^{\uparrow}|\psi_{\text{typ}}\rangle. \quad \text{(F6)}$$

We can interpret Eq. (F6) as corresponding to an average of $\hat{S}_n^z$ expectation values computed over (un-normalized) trajectories $|\overline{\psi_{n'}(t)}\rangle = \hat{\mathbb{U}}^t\hat{P}_{n'}^{\uparrow}|\psi_{\text{typ}}\rangle$ of random initial states, which subsequently have their n'-th site projected onto the spin-up state, and are then propagated in time by the repeated application of t Floquet unitary layers. This approach has two main advantages: it gives us a clear prescription for computing correlation functions given limited resources, and it provides an intuitive connection between the significance that correlation functions have with respect to transport due to the revelation that they are composed of initial excitations which then spread.

In this article, we restrict our analysis to systems with periodic boundary conditions, and - whilst individual circuits are not translationally invariant - we thus expect the transport properties to be translationally invariant given

sufficient realizations. Thus without loss of generality we set $n' = N/2$, and consider the magnetization profile:

$$M_n(t) = \frac{1}{\Lambda}\langle\overline{\psi_{N/2}}(t)|\hat{S}_n^z|\overline{\psi_{N/2}}(t)\rangle \approx \frac{1}{\Lambda}C_{n,N/2}(t) \quad \text{(F7)}$$

where $\Lambda = |\langle\overline{\psi_{N/2}}(0)|\overline{\psi_{N/2}}(0)\rangle|^2 \approx 1/2$ accounts for normalization of the initial state. Importantly, Eq. (F7) connects the magnetization profile to the correlation functions, which in turn encode information about transport. This approach offers a straightforward method for analyzing transport in large systems: generate a random state, project a single site onto the local spin-up state, dynamically evolve the state, and then probe the magnetization profile.

Due to our decision to interrogate systems with a $U(1)$ symmetry, we further insist that the initial typical state $|\psi_{\text{typ}}\rangle$ is drawn exclusively from a subsector of fixed magnetization $\langle\hat{S}_{\text{tot}}^z\rangle = M = \sum_n M_n(t)$. As discussed in the main text, we considered the zero-magnetization $M = 0$ subsector throughout. This is the largest possible subsector in the total space, with dimension $\binom{N}{N/2}$, and thus yields the most accurate typical-state trace estimation (as per our discussion of Eq. (F5)).

It is instructive to now determine the initial magnetization profile $M_n(0)$. The initial state $\frac{1}{\sqrt{\Lambda}}\hat{P}_{N/2}^{\uparrow}|\psi_{\text{typ}}\rangle$ is prepared as per the discussion of Eq. (F6) and Eq. (F7) and as discussed, for large systems it becomes a good approximation of Eq. (7).

Finally, we emphasize that a single realization of our model consists of (a) drawing a random state $|\psi_{\text{typ}}\rangle$ from which the initial state is generated, (b) generating spatial disorder embodied by drawing random phases $\{(\alpha_n, \beta_n, \phi_n)\}$, and (c) generating a random permutation $P(n)$ to define the circuit architecture. As per the typicality discussion above, the randomization over initial states is of negligible importance; we simply include it for completeness. The transport of the spin inhomogeneity at $n = N/2$, as captured by the magnetization profile $M_n(t)$, and the extraction of transport exponents are the foci of this study.

2. Dynamical correlation function in the M-subspace

The discussion can be adapted to our situation, where instead of working on the full Hilbert space, we limit it to $\mathcal{H}^{(M)}$. Let us define the dynamical correlation function restricted to the M-subspace as:

$$C_{n,N/2}^{(M)}(t) = \text{Tr}[\hat{P}_M\hat{S}_{N/2}^z(t)\hat{S}_n^z] \quad \text{(F8)}$$

where $\hat{P}_M = \sum_{i=0}^{d-1}|i_M\rangle\langle i_M|$ is the projector onto the magnetization subspace (with the basis $\{|i_M\rangle\}_{i=0}^{d-1}$). We can check how $C_{n,N/2}^{(M)}(t)$ is related to $C_{n,N/2}(t)$. Since

$\text{Tr}[\bullet] \equiv \sum_{M=-N/2}^{N/2} \text{Tr}[\hat{P}_M \bullet]$ we have:

$$C_{n,N/2}(t) = \sum_{M=-N/2}^{N/2} C_{n,N/2}^{(M)}(t). \qquad \text{(F9)}$$

We will see how to interpret $C_{n,N/2}^{(M)}(t)$ as the evolution of a perturbed initial state $\hat{\rho}(0)$, followed by a measurement, similarly as done for $C_{n,N/2}(t)$. We have defined the initial state as:

$$\hat{\rho}(0) = \hat{P}_M \left[|\uparrow\rangle\langle\uparrow|_{N/2} \otimes \left(\frac{\hat{\mathbb{I}}_2}{2} \right)^{\otimes(N-1)} \right] \hat{P}_M. \qquad (7)$$

We can notice that:

$$\text{Tr}[\hat{P}_M \hat{S}_n^z(t)] \overset{(1)}{=} \text{Tr}[\hat{P}_M \hat{S}_n^z]$$

$$\overset{(2)}{=} \frac{1}{N} \sum_{n=0}^{N-1} \text{Tr}[\hat{P}_M \hat{S}_n^z] \qquad \text{(F10)}$$

$$= \frac{1}{N} \text{Tr}[\hat{P}_M \hat{S}_{\text{tot}}^z] = \frac{M d_N^M}{N}$$

where (1): $[\hat{P}_M, \hat{\mathbb{U}}] = 0$ and (2): since $\hat{P}_M$ is invariant under permutation of spins, and $d_N^M = \binom{N}{\frac{N}{2}+M}$. Therefore

$$C_{n,N/2}^{(M)}(t) = \text{Tr}[\hat{P}_M \hat{S}_n^z(t) \hat{P}_{N/2}^{\uparrow}] - \text{Tr}[\hat{P}_M \hat{S}_n^z(t)]/2 \quad \text{(F11)}$$

becomes

$$C_{n,N/2}^{(M)}(t) = \text{Tr}[\hat{P}_M \hat{S}_n^z(t) \hat{P}_{N/2}^{\uparrow}] - \frac{M d_N^M}{2N}. \qquad \text{(F12)}$$

This eventually leads to:

$$C_{n,N/2}^{(M)}(t) = \text{Tr}[\hat{S}_n^z(t) \hat{\rho}(0)] - \frac{M d_N^M}{2N}$$
$$= M_n(t) - \frac{M d_N^M}{2N}. \qquad \text{(F13)}$$

3. Dynamical correlation function in the M-subspace through typicality

The last step remaining to connect $M_n(t)$ with the correlation functions involves typical states in the $\mathcal{H}^{(M)}$ space. In Ref. [8], it was shown how to calculate the (full space) dynamical correlation function $C_{n,N/2}(t) = \frac{1}{2^{N-2}} \text{Tr}[\hat{S}_n^z(t) \hat{S}_{N/2}^z(t)]$ by measuring an expectation value of a time-evolved typical random state. The basic idea is to use the fact that for a typical random state $|\psi_{\text{typ}}\rangle$, in a d-dimensional Hilbert space, we have:

$$\langle\psi_{\text{typ}}|\hat{A}|\psi_{\text{typ}}\rangle \simeq \frac{1}{d}\text{Tr}[\hat{A}] + O\left(\frac{1}{d}\right) \qquad \text{(F14)}$$

for any observable A (see also Ref. [77]), i.e., the trace of an operator is well approximated by taking its expectation value with respect to $|\psi_{\text{typ}}\rangle$. This is useful for

computing dynamical correlation functions because the expressions for $C_{n,N/2}(t)$ and $C_{n,N/2}^{(M)}(t)$ are expectation values $\text{Tr}[\hat{S}_n^z(t) \hat{\rho}_{N/2}(0)]$, where $\hat{\rho}_{N/2}(0) = \frac{1}{\tilde{d}}\hat{\mathbb{I}}_{\tilde{d}} \otimes \hat{P}_{n'}^{\uparrow}$ and $\tilde{d} = 2^{N-1}$ for $C_{n,N/2}(t)$, or $\tilde{d} = d' = \binom{N-1}{\frac{N-1}{2}+M-\frac{1}{2}}$ for $C_{n,N/2}^{(M)}(t)$. Such a trace can be computed via typical random states by:

$$\text{Tr}[\hat{S}_n^z(t) \hat{\rho}_{N/2}(0)] = \frac{1}{\tilde{d}}\text{Tr}\left[\hat{S}_n^z(t)\left(\hat{\mathbb{I}}_{\tilde{d}} \otimes \hat{P}_{n'}^{\uparrow}\right)\right]$$
$$= \frac{1}{\tilde{d}}\text{Tr}\left[\hat{S}_n^z(t) \hat{P}_{n'}^{\uparrow}\right] \qquad \text{(F15)}$$
$$\simeq \frac{d}{\tilde{d}}\langle\psi_{\text{typ}}|\hat{S}_n^z(t)|\psi_{\text{typ}}\rangle,$$

where d is the dimension of the space over which the trace is operating, i.e., $d = 2^N$ if its the full space $\Rightarrow \frac{d}{\tilde{d}} = \frac{2^N}{2^{N-1}} = 2$, or, $d = d_M^N = \binom{N}{\frac{N}{2}+M}$ if its a magnetization sub-sector $\Rightarrow \frac{d}{\tilde{d}} = \frac{d_M^N}{d_{M-\frac{1}{2}}^{N-1}} = \frac{N}{\frac{N}{2}+M}$. So, defining $|\psi_{\text{typ},N/2}\rangle = \hat{P}_{n'}^{\uparrow}|\psi_{\text{typ}}\rangle/\sqrt{|\langle\uparrow|_{N/2}|\psi_{\text{typ}}\rangle|^2}$ we have:

$$\text{Tr}[\hat{S}_n^z(t) \hat{\rho}_{N/2}(0)] \simeq \begin{cases} 2|\langle\uparrow|_{N/2}|\psi_{\text{typ}}\rangle|^2 \langle\psi_{\text{typ},N/2}|\hat{S}_n^z(t)|\psi_{\text{typ},N/2}\rangle, \\ \quad \text{if } |\psi_{\text{typ}}\rangle \text{ in full space} \\ \frac{N}{\frac{N}{2}+M}|\langle\uparrow|_{N/2}|\psi_{\text{typ}}\rangle|^2 \langle\psi_{\text{typ},N/2}|\hat{S}_n^z(t)|\psi_{\text{typ},N/2}\rangle \\ \quad \text{if } |\psi_{\text{typ}}\rangle \text{ in } M\text{-subspace} \end{cases}$$
$$\text{(F16)}$$

Finally, calculate:

$$|\langle\uparrow|_{N/2}|\psi_{\text{typ}}\rangle|^2 = \frac{1}{2}\left(\langle\psi_{\text{typ}}|\hat{S}_{N/2}^z|\psi_{\text{typ}}\rangle + 1\right)$$
$$= \begin{cases} \frac{1}{2} & \text{if } |\psi_{\text{typ}}\rangle \text{ in full space} \\ \frac{1}{2}\left(\frac{2M}{N}+1\right) & \text{if } |\psi_{\text{typ}}\rangle \text{ in } M\text{-subspace} \end{cases}$$
$$\text{(F17)}$$

so that:

$$\text{Tr}[\hat{S}_n^z(t) \hat{\rho}_{N/2}(0)] \simeq \langle\psi_{\text{typ},N/2}|\hat{S}_n^z(t)|\psi_{\text{typ},N/2}\rangle \qquad \text{(F18)}$$

in either scenario. Substituting into our equations for $C_{n,N/2}(t)$ and $C_{n,N/2}^{(M)}(t)$ gives:

$$C_{n,N/2}(t) = \text{Tr}[\hat{S}_n^z(t) \hat{\rho}_{N/2}(0)] = \langle\psi_{\text{typ},N/2}|\hat{S}_n^z(t)|\psi_{\text{typ},N/2}\rangle$$
$$\text{(F19)}$$

with $|\psi_{\text{typ},N/2}\rangle$ in full space and

$$C_{n,N/2}^{(M)}(t) = \gamma\text{Tr}[\hat{S}_n^z(t) \hat{\rho}_{N/2}(0)] - \eta$$
$$= \gamma\langle\psi_{\text{typ},N/2}|\hat{S}_n^z(t)|\psi_{\text{typ},N/2}\rangle - \eta$$
$$\text{(F20)}$$

with $|\psi_{\text{typ},N/2}\rangle$ in M-subspace.